PALEOCEANOGRAPHY, VOL. 23, PA4208, doi:10.1029/2008PA001592, 2008

How important are Southern Hemisphere wind changes for low glacial carbon dioxide? A model study

T. Tschumi,[1] F. Joos,[1,2] and P. Parekh[1]

Received 14 January 2008; revised 4 July 2008; accepted 14 August 2008; published 31 October 2008.

[1] The response of atmospheric CO_2 to modifications in the strength and position of Southern Hemisphere westerlies is examined with the Bern3D ocean model. The model responds more sensitively to changes in the wind amplitude than to variations in latitudinal position. Depending on the model setup, a 50% reduction in wind strength leads to a CO_2 drawdown of 3–34 ppm, while a 50% increase results in a rise of 10–24 ppm. A poleward shift of 5° lowers CO_2 by 2–16 ppm whereas an equatorward shift of 5° induces a CO_2 increase of 2–14 ppm. Physical and biological mechanisms equally contribute to the modeled changes in atmospheric CO_2. Our results are in conflict with the hypothesis that Southern Hemisphere wind changes are responsible for the low atmospheric CO_2 concentrations during glacial periods.

Citation: Tschumi, T., F. Joos, and P. Parekh (2008), How important are Southern Hemisphere wind changes for low glacial carbon dioxide? A model study, *Paleoceanography*, *23*, PA4208, doi:10.1029/2008PA001592.

1. Introduction

[2] In spite of more than 20 years of research, the causes of glacial-interglacial fluctuations in atmospheric CO_2 still remain an unresolved issue. Many potentially important mechanisms have been suggested [e.g., *Archer et al.*, 2000a; *Sigman and Boyle*, 2000], but sparse paleodata and limitations of currently applied models impede an unequivocal identification of the relevant processes. It is well established, however, that the atmospheric CO_2 variations are the result of the redistribution of carbon between the terrestrial, oceanic and atmospheric reservoirs.

[3] In this study, we focus on the role of the Southern Hemisphere westerly winds (SHW) in regulating the large-scale ocean circulation and the ocean's carbon storage capacity. Our goal is (1) to assess the sensitivity of the large-scale ocean circulation, implied biogeochemical changes and the response in atmospheric CO_2 to a modified strength and position of the SHW and (2) to discuss their potential role in explaining glacial-interglacial CO_2 fluctuations.

[4] *Toggweiler et al.* [2006] suggest that a feedback between SHW, ocean circulation and atmospheric CO_2 is largely responsible for glacial-interglacial CO_2 fluctuations. The proposed mechanism is based on the concept that the global large-scale overturning circulation can be split into two different regimes that occupy distinct domains in the ocean interior [*Toggweiler et al.*, 2006, Figure 3]. Their northern regime corresponds to the "biologically productive North Atlantic circuit" that is filled with NADW (North Atlantic Deep Water). The southern regime is the "unproductive Southern Ocean circuit," i.e., the domain of AABW (Antarctic Bottom Water). Sinking organic particles are remineralized at depth in both circuits. When the water of the southern circuit comes up to the surface in the Southern Ocean (SO) today, the remineralized carbon escapes fairly easily to the atmosphere. In contrast, relatively little remineralized carbon escapes from the surface waters of the biologically productive northern circuit since biological production draws down surface pCO_2.

[5] *Toggweiler et al.*'s [2006] view of the glacial ocean is a scenario where the northern circuit remains active while the southern circuit is weak leading to a buildup of respired CO_2 in the deep ocean and to less CO_2 outgassing from the SO. In their hypothesis, *Toggweiler et al.* [2006] attach critical importance to the position of the SHW. They argue that the glacial SHW were equatorward of their present position such that upwelling next to Antarctica was suppressed and the southern circuit was essentially shut off during glacial times.

[6] Several recent studies show that SH winds modify large-scale overturning and air-sea CO_2 fluxes in the SO on decadal time scales. Observations and models indicate a poleward intensification in the SHW during recent decades [*Thompson and Solomon*, 2002; *Gillett and Thompson*, 2003], which has resulted in an enhanced wind-driven upwelling around Antarctica [*Russell et al.*, 2006; *Lovenduski and Gruber*, 2005; *Hall and Visbeck*, 2002]. *Lovenduski et al.* [2007] propose that this has led to an anomalous uptake of anthropogenic CO_2 but to an even larger anomalous outgassing of natural CO_2 over the SO. Therefore, higher stabilization levels of atmospheric CO_2 would have to be expected on a multicentury time scale if the trend persists in the future [*Le Quéré et al.*, 2007].

[7] In this study, we will revisit Toggweiler's glacial-interglacial hypothesis testing its feasibility in the Bern3D coarse-resolution model [*Müller et al.*, 2006; *Parekh et al.*,

[1]Climate and Environmental Physics, Physics Institute, University of Bern, Bern, Switzerland.
[2]Also at Oeschger Centre for Climate Change Research, University of Bern, Bern, Switzerland.

0883-8305/08/2008PA001592$12.00

Table 1. Different Model Setups[a]

Setup	$F_{Atl\text{-}Pac}$ (Sv)	κ_{dia} (10^{-5} m^2 s^{-1})	BC	NUE (%)	CEE (%)
RBC	0.0	3.5	restoring	73.8	10.2
weakFw	0.0	3.5	mixed	74.4	9.5
standard	0.20	3.5	mixed	70.9	9.5
strongFw	0.40	3.5	mixed	67.4	9.4
RBC lowdiff	0.0	1.0	restoring	80.9	12.3
weakFw lowdiff	0.0	1.0	mixed	80.8	12.4
lowdiff	0.15	1.0	mixed	79.3	12.6
strongFw lowdiff	0.30	1.0	mixed	78.3	13.1

[a]The amount of the Atlantic to Pacific freshwater flux ($F_{Atl\text{-}Pac}$), the value of diapycnal diffusivity (κ_{dia}) and the boundary conditions (BC) employed along with simulated global nutrient utilization efficiency (NUE) and global $CaCO_3$ cycle efficiency (CEE) (as defined in section 3.3) at steady state for standard wind stress.

2008]. It is tested whether an equatorward shift in the latitudinal position of the SHW can substantially reduce deep ocean ventilation and whether a shutdown of the southern circuit results in lower atmospheric CO_2. Furthermore, Toggweiler's study is extended regarding two important issues. In their modeling study, *Toggweiler et al.* [2006] do not explicitly shift the SHW in order to test their hypothesis. Instead they weaken the SHW arguing that this would have essentially the same effect on upwelling in the SO as an equatorward wind displacement. Here, both the effect of changing the strength of the westerlies, as well as the response to an explicit shift in the position of the westerlies are investigated. Second, to avoid changes in nutrient utilization upon circulation changes, *Toggweiler et al.* [2006] simulate the production of sinking organic particles and $CaCO_3$ by restoring surface phosphate concentrations toward a fixed field. In addition to model runs with this same procedure, we also perform simulations with a prognostic formulation of marine biogeochemistry. This enables us to quantitatively analyze contributions from physical as well as biogeochemical processes (section 3.3).

[8] A series of different wind stress scenarios spanning the entire range of available reconstructions for glacial SH winds was created to generally test the model's sensitivity to marine carbon cycling and atmospheric CO_2 (section 2.3). In a first set of experiments we probe the model response to a change in the SH westerlies' amplitude and compare the results with the findings of previous studies [*De Boer et al.*, 2008; *Toggweiler et al.*, 2006; *Toggweiler and Samuels*, 1995]. In a second set we explore the effect of an explicit latitudinal shift in the SH westerlies' position to find out whether the model behaves similarly as in the case of modified wind strength.

[9] In order to examine the robustness of the model response with respect to different initial states, we impose the various scenarios on 8 model setups (Table 1) that differ with respect to the type of boundary conditions, the strength of diapycnal mixing, the rate of Atlantic meridional overturning and the strength of the carbon "pumps" [*Volk and Hoffert*, 1985].

[10] We finally carry out additional model sensitivity tests examining the effect on atmospheric CO_2 induced by (1) increased CO_2 solubility, (2) reduced gas exchange in the SO due to enlarged sea ice cover, (3) $CaCO_3$ compensation, and (4) a 500 GtC carbon input into the atmosphere. In this last set of simulations we separately and jointly impose these four mechanisms on a model state in which atmospheric CO_2 is lowered in response to weakened SHW.

[11] The cost-efficient, dynamical, three-dimensional Bern3D ocean model [*Müller et al.*, 2006] allows for an adequate representation of the large-scale ocean circulation and the cycling of major biogeochemical tracers (section 2.2). Its computational efficiency makes it ideally suited for multimillennial paleosimulations and large ensembles of sensitivity simulations.

2. Methods

2.1. Model Description

[12] The physical core of the Bern3D model is a frictional-geostrophic balance ocean model [*Müller et al.*, 2006; *Edwards and Marsh*, 2005]. Model grid resolution is 36 by 36 cells in the horizontal and 32 vertical layers with exponentially increasing thickness toward the ocean bottom. The model includes an isopycnal diffusion scheme and Gent-McWilliams parametrization for eddy-induced transport [*Griffies*, 1998]. Convection is represented in the model by shifting down statically unstable water parcels from the surface further downward in the water column according to the density of the parcel. Subsequently, tracer concentrations are homogenized over remaining regions of static instability in the water column.

[13] Sea surface temperatures (SST) and salinities (SSS) are constrained by using either restoring (RBC) or mixed boundary conditions (MBC). Restoring compels SST and SSS to remain close to modern-day observational values. MBC on the other hand prescribe freshwater fluxes on the ocean surface rather than SSS such that circulation-salinity feedbacks are allowed to develop upon perturbation of the model state [*Bryan*, 1986]. An additional uniform freshwater surface flux from the Atlantic to the Pacific basin is applied in order to intensify and deepen the Atlantic MOC. Forcing fields for wind stress are based on a simple analytical profile that is zonally and temporally uniform (section 2.3). Here, meridional wind stress is neglected as in the work by *Toggweiler et al.* [2006]. Standard values for diapycnal diffusivity κ_{dia} and for the Atlantic-Pacific freshwater surface flux $F_{Atl\text{-}Pac}$ have been selected to reproduce a realistic meridional overturning circulation as well as a realistic radiocarbon distribution on a basin-wide scale (Figure 1a). The application of analytical wind stress

Figure 1. Standard model state: (a–e) Basin-averaged annual mean depth profiles for natural $\Delta^{14}C$, phosphate, dissolved inorganic carbon, alkalinity, and silicic acid. Solid lines correspond to modeled profiles. Dotted lines are data-based estimates from GLODAP ($\Delta^{14}C$, DIC, alkalinity [*Key et al.*, 2004]) and World Ocean Atlas 2001 (phosphate, silicic acid [*Conkright et al.*, 2002]). (f) Basin-averaged profiles for $\Delta C_{gas\text{-}ex}$ (dotted lines), $\Delta C_{gas\text{-}ex} + \Delta C_{carb}$ (dashed lines), and $\Delta C_{gas\text{-}ex} + \Delta C_{carb} + \Delta C_{soft}$ (solid lines) following *Gruber and Sarmiento* [2002]. Black lines are based on model output, and red lines are calculated from data. Global mean surface values are set to zero for modeled and for data-based profiles.

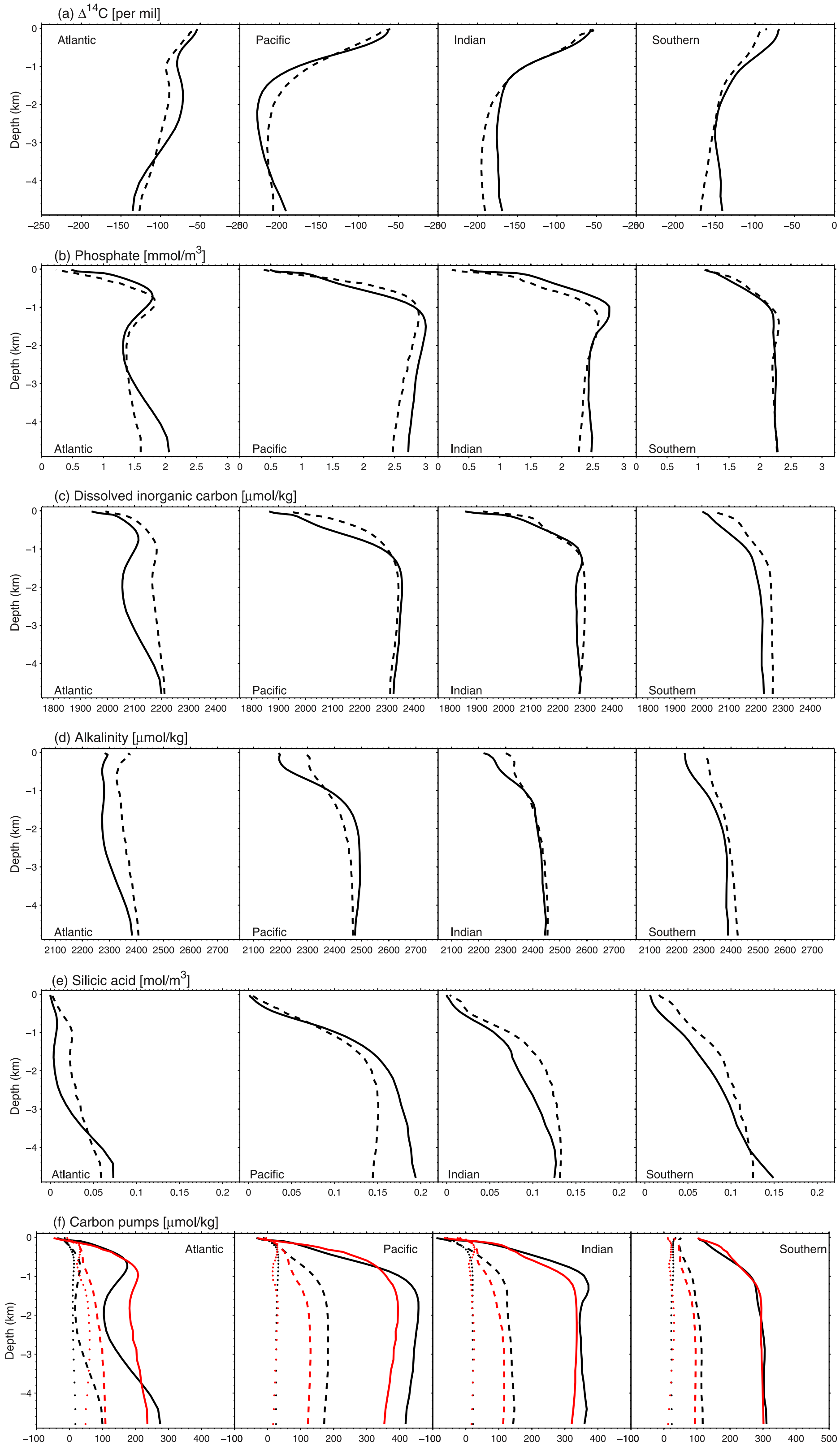
(a) Δ14C [per mil]
Atlantic
Pacific
Indian
Southern
Depth (km)
(b) Phosphate [mmol/m3]
(c) Dissolved inorganic carbon [μmol/kg]
(d) Alkalinity [μmol/kg]
(e) Silicic acid [mol/m3]
(f) Carbon pumps [μmol/kg]

Figure 1

Table 2. Model Parameters With Their Standard Values and References

Parameter	Description	Value	Reference
K_I	isopycnal diffusivity	1000 $m^2\ s^{-1}$	*Müller et al.* [2006]
K_{GM}	Gent-McWilliams parameter	2000 $m^2\ s^{-1}$	*Müller et al.* [2006]
K_D	diapycnal diffusivity	$3.5 \times 10^{-5}\ m^2 s^{-1}$	this study
$z_{euphotic}$	depth of euphotic zone	75 m	OCMIP-2
σ	DOM fraction	$\frac{2}{3}$	OCMIP-2
α	POM remineralization Martin-scale	0.9	OCMIP-2
κ_{PO4}	half-saturation constant for PO_4	0.05 μM PO_4	*Parekh et al.* [2008]
κ_{Fe}	half-saturation constant for *Fe*	0.17 nM Fe	*Parekh et al.* [2008]
τ	biomass turnover time scale	30 days	*Parekh et al.* [2008]
$\mathcal{R}_{C:P}$	Redfield ratio C:P	117	*Anderson and Sarmiento* [1994]
$\mathcal{R}_{N:P}$	Redfield ratio N:P	16	*Anderson and Sarmiento* [1994]
$\mathcal{R}_{O2:P}$	Redfield ratio O_2:P	−170	*Anderson and Sarmiento* [1994]
$\mathcal{R}_{Fe:P}$	ratio Fe:P	5.85×10^{-4}	*Parekh et al.* [2008]
l_{opal}	opal redissolution length scale	10,000 m	*Heinze et al.* [1999]
$l_{calcite}$	calcite redissolution length scale	3500 m	OCMIP-2
$K^{D,min}_{Si}$		10^{-3} mol m^{-3}	*Aumont and Bopp* [2006]
$K^{D,max}_{Si}$		7×10^{-3} mol m^{-3}	*Aumont and Bopp* [2006]
K^{D*}_{Si}	half-saturation constant for Si/C increase	5×10^{-3} mol m^{-3}	*Aumont and Bopp* [2006]
$R^{*}_{Si:P}$		30 mol Si/mol P	this study
$R_{Ca:P}$	Ca:P uptake ratio in calcifiers	0.3 mol Ca/mol P	this study
M_{CaCO3}	maximum rain ratio	0.3	this study

profiles in this specific study as opposed to the NCEP wind stress data applied in other Bern3D studies [*Müller et al.*, 2008; *Siddall et al.*, 2007; *Parekh et al.*, 2008; M. Gerber et al., Regional air-sea fluxes of anthropogenic carbon inferred with an Ensemble Kalman Filter, submitted to Global Biogeochemical Cycles, 2008] required an upward adjustment of κ_{dia} from 1.0 to 3.5×10^{-5} m^2 s^{-1}. Standard parameter values for the physical and biogeochemical model are summarized in Table 2.

[14] The biogeochemical component of the Bern3D model represents the cycling of dissolved inorganic carbon (DIC), dissolved organic phosphate (DOP), ^{14}C, alkalinity, phosphate, oxygen, iron and silicic acid. The ocean carbon cycle is coupled to a well-mixed atmospheric reservoir of CO_2. The formulations for air-sea gas exchange and carbonate chemistry in the ocean are based on the updated OCMIP-2 protocols [*Orr et al.*, 1999; *Najjar and Orr*, 1999] and include adaptations as described by *Müller et al.* [2008]. Fully prognostic formulations are used to compute export production of organic matter, biogenic opal and $CaCO_3$ (see auxiliary material).[1]

2.2. Model Evaluation

[15] The cost-efficient Bern3D model is able to capture the large-scale ocean circulation (Figure 2), the characteristics of the most important water masses, the large-scale distributions of a range of ventilation time scale tracers (^{14}C, CFCs, ^{39}Ar, anthropogenic carbon [see *Müller et al.*, 2006]), biogeochemical tracers, temperature and salinity (Figure 1 and Table 3), as well as the spatial patterns of POM, $CaCO_3$ and opal export production for standard parameter values. The results presented in the following two subsections have been obtained using the standard model parameter values (Table 2) and the standard analytical wind stress profile (section 2.3).

2.2.1. Meridional Overturning Circulation and Water Masses

[16] The global annual mean residual overturning circulation (Figure 2a) in the deep ocean displays the clockwise overturning cell in the north driven by the formation of NADW and the anticlockwise cell in the south associated with the formation of AABW. The middepth NADW cell can be interpreted as the "northern biologically productive circuit" and the deep anticlockwise overturning can be associated with the "southern unproductive circuit" as described by *Toggweiler et al.* [2006]. Deep convection occurs predominantly in the North Atlantic area south of Greenland (NADW) as well as in the Ross and Weddell Seas next to Antarctica (AABW). Maximum overturning in the Atlantic (Figure 2b) reaches 21.7 Sv at around 55°N comparable to the estimate of *Talley et al.* [2003] of 17 ± 5 Sv. 14.8 Sv of this southward flow are exported from the Atlantic into the SO at 30°S. A weak anticlockwise overturning cell with a maximum of 2.4 Sv fills the deepest parts of the Atlantic with AABW. Overturning in the deep Pacific (Figure 2c) is anticlockwise and amounts to a maximum of 9.8 Sv, 4.8 Sv of which recirculate back into the SO. Deep equatorial upwelling in the Pacific amounts 5 Sv, relatively modest for a coarse-resolution model.

[17] A comparison between modeled and data-based salinity and natural radiocarbon zonal mean sections in the Atlantic and the Pacific reveals that overall surface-to-deep transport and the primary flow paths of the most important water masses are represented quite realistically in the model (not shown). The observed NADW tongue of relatively salty and young waters in the North Atlantic is clearly established in the model. Compared to data-based distributions, modeled NADW seems to be too young in $\Delta^{14}C$ by about 20 per mil. The northward flowing Antarctic Intermediate Water (AAIW) in the Atlantic is modeled as a

[1]Auxiliary materials are available in the HTML. doi:10.1029/2008PA001592.

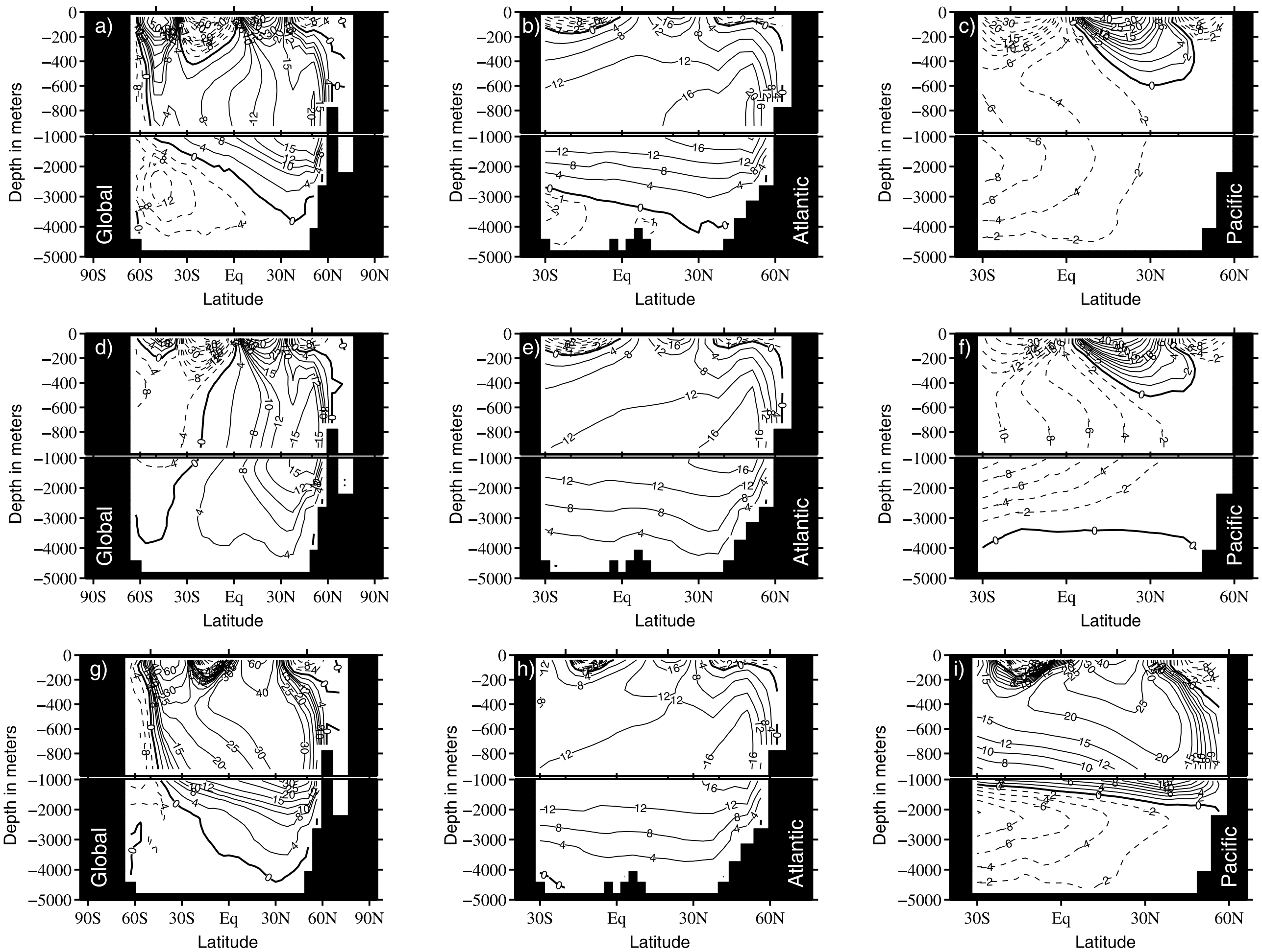

Figure 2. Annual mean residual overturning circulation (Sv) in the global, Atlantic, and Pacific ocean for the standard model configuration. (a–c) The circulation for the case of standard (modern) winds and (d–f) the results for SH westerlies with a fourfold reduced amplitude. (g–i) The case of SH westerlies that are shifted by 10° toward the equator. The stream functions include the contribution resulting from Gent-McWilliams transport. Continuous (dashed) contours are for positive (negative) values.

relatively fresh water mass lying above NADW. The deep Atlantic is filled with AABW. Horizontal radiocarbon gradients in the deep Pacific are relatively well captured in the model, however, the water in the deep North Pacific is somewhat too old. AAIW penetrates the Pacific basin from surface to a depth of about 1 km.

2.2.2. Tracer Distributions and Biological Export Fluxes

[18] The Bern3D model is able to adequately represent basin-scale surface-to-deep gradients for a range of different tracers (Figure 1). The modeled tracer distributions correlate reasonably well with observed fields interpolated to the model grid (Table 3). Simulated zonal mean sections in the Atlantic and the Pacific generally compare favorably with observations (e.g., Figures 3a and 3b). Modeled export fluxes for POM (15.9 GtC a^{-1}), $CaCO_3$ (1.4 GtC a^{-1}) and opal (97.6 TmolSi a^{-1}) are compatible with observation-based estimates [*Falkowski et al.*, 1998; *Iglesias-Rogdríguez et al.*, 2002; *Treguer et al.*, 1995]. Their spatial patterns (Figures 3c and 3d) display the prominent large-scale features of the observed fields. However, because of imperfections in the model circulation, POM and $CaCO_3$ export in the North Pacific are underestimated [*Schlitzer*, 2000].

Table 3. Correlations and Relative Standard Deviations of Modeled Tracer Fields in the Standard Model Setup in Comparison to Data-Based Fields

Tracer	Correlation With Data	Relative Standard Deviation	Data Source
Temperature	95.2%	0.97	*Levitus and Boyer* [1994]
Salinity	79.2%	1.37	*Levitus et al.* [1994]
$\Delta^{14}C$	94.9%	1.18	*Key et al.* [2004]
Phosphate	88.9%	1.03	*Conkright and Boyer* [2002]
Preindustrial DIC	91.8%	1.41	*Key et al.* [2004]
Alkalinity	92.3%	1.80	*Key et al.* [2004]
Silicic acid	90.4%	1.30	*Conkright and Boyer* [2002]

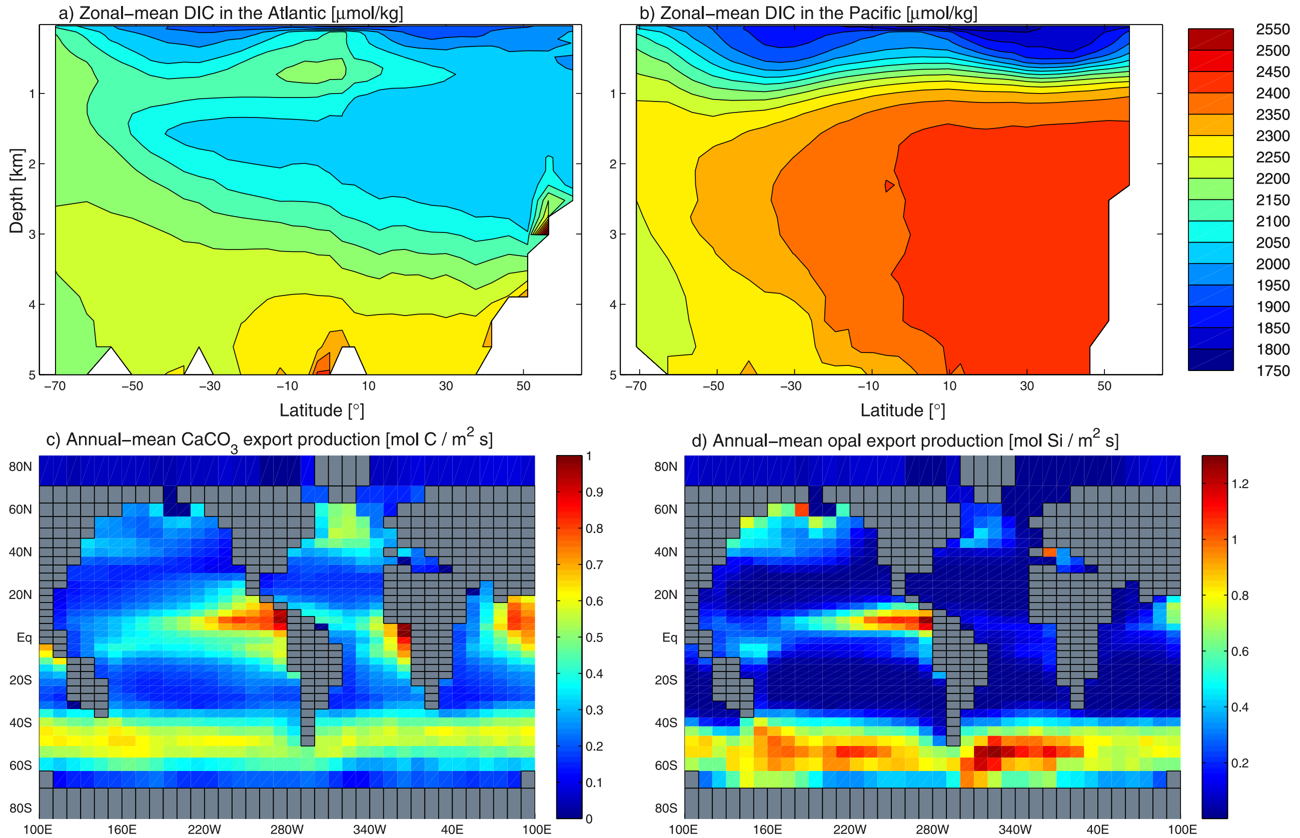

Figure 3. Standard model state: Zonal mean DIC distribution (μmol kg^{-1}) in (a) the Atlantic and (b) the Pacific. (c) Annually averaged $CaCO_3$ export production (mol C m^{-2} s^{-1}) and (d) opal export production (mol Si m^{-2} s^{-1}). Total yearly export productions of 1.4 GtC a^{-1} for $CaCO_3$ and 97.6 Tmol Si a^{-1} for opal are comparable to available estimates.

[19] Figure 1c shows that basin-wide surface-to-deep gradients in DIC are reasonably well simulated in the Bern3D model. The question remains, however, whether the three main processes responsible for shaping the spatial distribution of DIC in the ocean, namely the organic matter cycle, the $CaCO_3$ cycle and the air-sea gas exchange, do contribute in realistic proportions to the modeled gradients. *Gruber and Sarmiento* [2002] introduced the three tracers ΔC_{soft}, ΔC_{carb} and $\Delta C_{gas\ ex}$ in order to assess their relative importance. ΔC_{soft} and ΔC_{carb} quantify the impact of the organic matter and $CaCO_3$ cycles in absence of gas exchange. $\Delta C_{gas\ ex}$ represents the residual part of the gradients in the salinity-normalized DIC distribution. Figure 1f displays simulated and data-based depth profiles of ΔC_{soft}, ΔC_{carb} and $\Delta C_{gas\ ex}$. Both positive and negative deviations for the observation-based profiles are simulated for the individual tracers. The comparison indicates that the relative strengths of the three processes are reasonably simulated.

[20] $\Delta C_{gas\ ex}$ is the sum of two opposing contributions $\Delta C^{bio}_{gas\ ex}$ and $\Delta C^{therm}_{gas\ ex}$ arising from biological processes and thermal fluxes, respectively. The net surface-to-deep gradients in $\Delta C_{gas\ ex}$ are therefore comparatively small (see Figure 1f). Note that the surface-to-deep gradient in the $\Delta C^{therm}_{gas\ ex}$ corresponds to the solubility pump as defined by *Volk and Hoffert* [1985]. There is an ongoing debate in the literature about how realistically the solubility pump is represented in current ocean models [e.g., *Broecker et al.*, 1999; *Archer et al.*, 2000b; *Toggweiler et al.*, 2003] It seems that in OGCMs the solubility pump is subject to a rather strong kinetic limitation by air-sea gas exchange. On the other hand, in box models the kinetic limitation seems to be much weaker [*Toggweiler et al.*, 2003]. Unfortunately, it is currently not possible to estimate $\Delta C^{therm}_{gas\ ex}$ and thus the real strength of the solubility pump directly from data [*Sarmiento and Gruber*, 2006]. However, there are accurate data-based estimates available for the potential strength of the solubility pump, i.e., for the case with infinitely rapid gas exchange.

[21] Next, we assess how the Bern3D model represents the solubility and the potential solubility pump to place the model in the current discussion. This is done by running the model in a setup without marine biota using standard gas exchange transfer velocities in a first experiment; in a second experiment transfer velocities are increased by a factor of fifteen. The two simulations yield surface-to-deep gradients of 91 μmol kg^{-1} and 154 μmol kg^{-1}, respectively. The latter value is in very good agreement with the data-based estimate of 155 μmol kg^{-1} by *Sarmiento and Gruber* [2006] for the potential solubility pump. In the Bern3D model, we simulate a deviation of 63 μmol kg^{-1} between the realized and the potential solubility pump. *Toggweiler et al.* [2003] suggest in their concluding section that this deviation should be about 50 μmol kg^{-1} in the real ocean.

These gradients and differences in gradients may also be compared with the overall preindustrial surface-to-deep DIC gradient of about 305 μmol kg^{-1}. Uncertainties in the model representation of the solubility pump remain, as long as its real strength cannot be well quantified by observations.

2.3. Wind Stress Scenarios

[22] The reconstruction of past wind circulation from indirect proxy indicators is a complex task. The interpretation of Late Quaternary paleoenvironmental records from South America and Australia has therefore led to conflicting claims about the latitudinal position of the SHW at the LGM. One school argues for equatorward shifted westerlies [*Moreno et al.*, 1999; *Heusser*, 1989] and another supports poleward shifted westerlies [*Markgraf*, 1989; *Harrison and Dodson*, 1993]. In a review of multiple proxy indicators [*Shulmeister et al.*, 2004] come to the conclusion that there is good evidence for enhanced westerly flow and increased wind-driven upwelling at the LGM and that glaciation-interglaciation shifts were no more than 3° to 4°.

[23] Model results are also contradictory regarding the nature of SHW at the LGM. Some of them indicate a general intensification and a poleward displacement of their zonal maximum [*Wyrwoll et al.*, 2000], and some suggest a weakening and a slight equatorward shift [*Kim et al.*, 2002]. Others point at no significant latitudinal shift with either a modest weakening [*Rojas et al.*, 2008] or a slight strengthening of the wind stress over the SO [*Otto-Bliesner et al.*, 2006]. In light of the large gaps in the quantitative and qualitative understanding of the SH wind circulation at the LGM, we created a variety of scenarios that span the entire range of available reconstructions.

[24] All the wind stress scenarios are based on an analytical profile. For simplicity, the meridional wind stress component is neglected and the zonal component τ^λ is zonally and temporally uniform. The profile's mathematical expression is a function of two parameters ϵ and μ that allow for the scaling of the SH westerlies' amplitude and for a latitudinal shift in the SH wind stress profile, respectively:

$$\tau^\lambda(\phi) = \begin{cases} 0.2 + 0.8\sin\left[6(\phi + 4 - \mu)\right] \\ \quad \forall\, \phi \in [-80, -64 - \delta + \mu] \\ \quad \cup\, (-34 + \delta + \mu, -19 + \mu], \\ \\ \epsilon 1.6\{0.2 + 0.8\sin\left[6(\phi + 4 - \mu)\right]\} \\ \quad \forall\, \phi \in (-64 - \delta + \mu, -34 + \delta + \mu], \\ \\ 0.25\cos\left[\frac{360}{38-\mu}\left(\phi - \frac{\mu}{2}\right)\right] - 0.35 \\ \quad \forall\, \phi \in (-19 + \mu, 19], \\ \\ 0.2 + 0.8\sin\left[6(4 - \phi)\right] \\ \quad \forall\, \phi \in (19, 80], \\ \\ \text{with } \delta = \frac{1}{6}\arcsin\left(\frac{1}{4}\right). \end{cases} \tag{1}$$

[25] Figure 4a shows that the standard profile (ε = 1.0, μ = 0) reasonably reproduces the zonally and seasonally averaged zonal component of the NCEP reanalysis derived data [*Kalnay et al.*, 1996].

[26] We created two ensembles of scenarios by modifying either ε or μ with respect to their standard values. In the first ensemble (scaling scenarios) the SHW are weakened and intensified without altering their location by setting ϵ to 0.25, 0.5, 0.75, 1.5, 2.0 and 3.0 (Figure 4a). In the second ensemble (shift scenarios) we shift the position of the SH westerlies' peak poleward as well as equatorward (Figure 4c). Maximal latitudinal displacements are 5° toward the South Pole (μ = −5) and 10° toward the equator (μ = 10). The intermediate displacement scenarios are spaced by 1°.

[27] The Ekman pumping strength quantifies wind-driven upwelling, which corresponds to the degree of divergence of wind-driven horizontal flows in the sea surface. Wind-driven upwelling in the open ocean is generally limited to a surface layer some hundreds of meters thick. In the SO, however, the absence of the geostrophic balance above topographic ridges leads to a situation where deep water is brought to the surface through the action of winds. The Ekman pumping strength, integrated from 90°S, is depicted in Figures 4b and 4d for the different wind stress scenarios.

2.4. Model Setups and Spin-Up

[28] Although the performance of the Bern3D model regarding the representation of the modern ocean is quite reasonable (section 2.2), there still remains some degree of uncertainty due to the limited spatial coverage of the observations needed to test the model and due to the interpretation of indirect measurements. For this reason, the wind stress scenarios are imposed on 8 different setups to assess the robustness of the model response. As summarized in Table 1 the model setups differ in the type of boundary conditions (restoring versus mixed), the value for diapycnal diffusivity κ_{dia} and the intensity of the anomalous surface freshwater flux $F_{Atl\text{-}Pac}$ from the Atlantic to the Pacific basin.

[29] The driving forces of the meridional overturning circulation (MOC) are still a matter of intense investigation. Presently, two major mechanisms are discussed [*Kuhlbrodt et al.*, 2007]. The first one is turbulent mixing of heat from the surface into the ocean's interior, the second is wind-driven upwelling in the Southern Ocean. From this perspective, the choice of diapycnal diffusivity κ_{dia} controls the relative importance of thermohaline versus wind-driven MOC forcing in a given model setup.

[30] The sinking of dense, salty water in the North Atlantic is an important organizing feature of the modern deep ocean circulation. Modeled deep water mass properties, ventilation time scales and tracer distributions in different ocean basins are quite sensitive to the modeled rate of deep water formation in the North Atlantic. The anomalous surface freshwater flux $F_{Atl\text{-}Pac}$ permits a systematical increase (decrease) in Atlantic sea surface salinities and a strengthening (weakening) of the Atlantic MOC.

[31] For every model setup a steady state has been computed in the following manner: First, the physical model is spun-up for 10,000 model years using RBC.

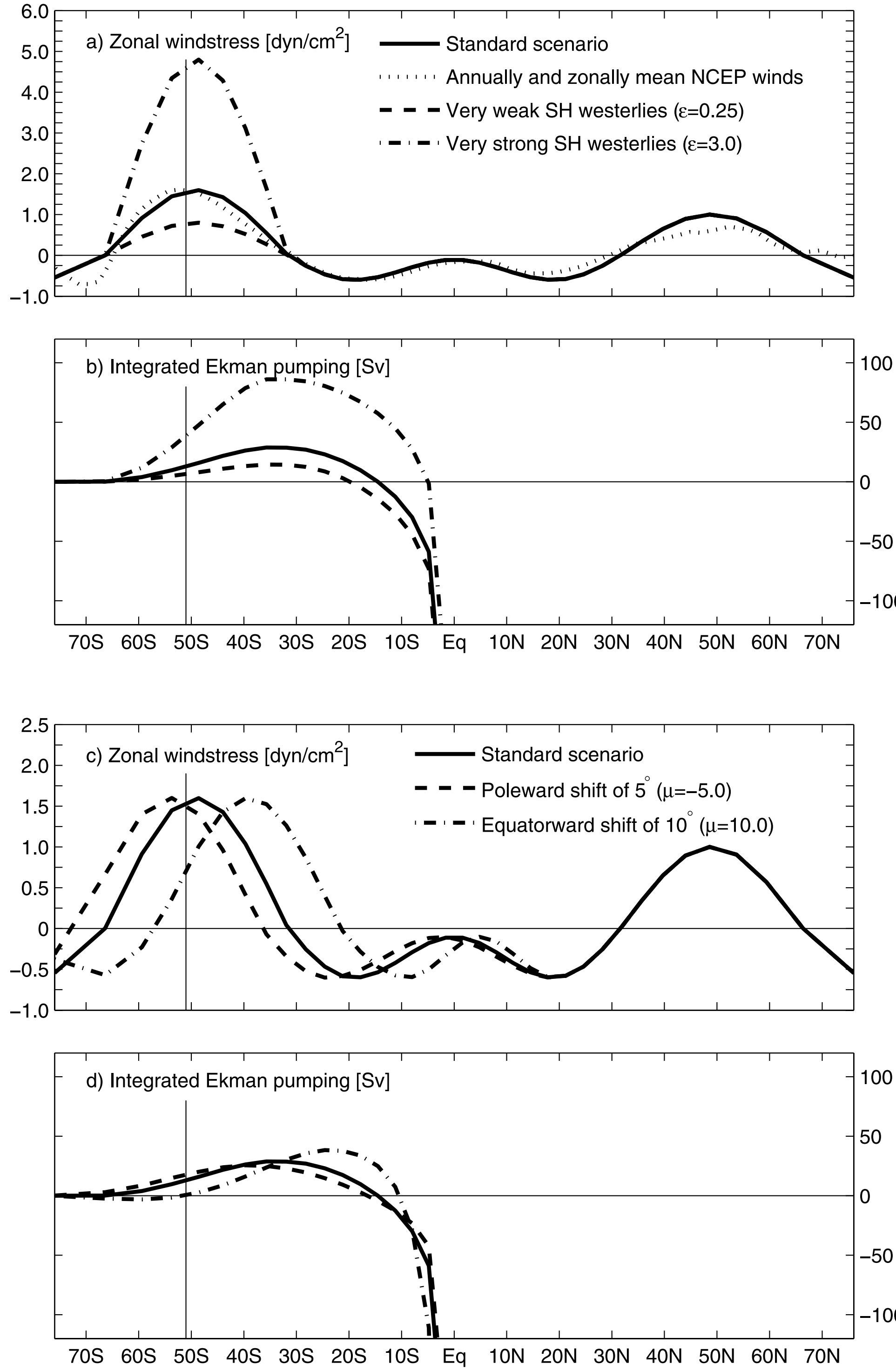

Figure 4. The wind stress scenarios and the associated Ekman pumping: (a and b) scaling scenarios and (c and d) shift scenarios. The vertical solid lines at 51°S indicate the location of the tip of South America in the model geometry which corresponds to the northern border of the Southern Ocean.

Subsequently, air-sea freshwater fluxes are diagnosed and averaged over the last 1000 years to provide mixed boundary conditions. The model is now switched to mixed boundary conditions and anomalous freshwater fluxes $F_{Atl\text{-}Pac}$ are included. In the case of the setups that employ restoring, by definition RBC are maintained and no additional freshwater flux $F_{Atl\text{-}Pac}$ is applied. Then, a biogeochemical spin-up phase with a fixed atmospheric CO_2 mixing ratio of

278 ppm is run for another 10,000 years. Thereafter, atmospheric CO_2 is allowed to evolve freely. Annual means are used for the analysis.

2.5. Overview of Experiments

[32] In the first set of experiments we impose the scaling scenarios on a spun-up model state by instantaneously switching from the standard to a modified wind stress profile. The model is then run into a new steady state over 5000 model years. The gas transfer velocity field is kept unchanged upon wind stress perturbation. The second set consists of corresponding experiments employing the shift scenarios. Each of the wind stress scenarios is applied to the 8 different setups of the model. The CO_2 response in simulations where the SHW are both scaled and shifted simultaneously is essentially the superposition of the responses that are induced by the wind scaling and the shift separately. Such experiments with changes in both position and strength will not be further discussed. In a third set of experiments we investigate the additional effects of enhanced glacial CO_2 solubility, increased sea ice cover to gas exchange, $CaCO_3$ compensation and terrestrial carbon release with respect to atmospheric CO_2. A 500 GtC carbon input from the terrestrial biosphere [e.g., *Shackleton*, 1977] is represented by instantaneously increasing atmospheric CO_2 by 236 ppm. Enhanced CO_2 solubility is modeled by imposing a reconstruction of LGM SST and SSS [*Paul and Schäfer-Neth*, 2003] on the carbonate chemistry routine that calculates the speciation of DIC and pCO_2 in the sea surface. Reduced gas exchange from increased sea ice cover is represented by linearly scaling down piston velocities according to a monthly map of fractional sea ice cover for the LGM [*Paul and Schäfer-Neth*, 2003]. To simulate $CaCO_3$ compensation the CO_3^{2-} concentration in each bottom ocean cell below 2000 m is restored toward the CO_3^{2-} value diagnosed in the unperturbed state. This approach allows for both sediment dissolution and accumulation leading to an addition or removal of alkalinity and DIC in a 2:1 ratio. Starting from the initial state lowdiff, we perform another five simulations where, in addition to a halving of the SH westerlies' amplitude, the four additional mechanisms are taken into account separately and jointly. Each configuration is run into a new steady state during a period of 10,000 model years. A more detailed description of how the additional mechanisms are represented in this study can be found in the auxiliary material.

3. Model Results

3.1. Scaling Experiments

3.1.1. Ocean Circulation and Ventilation

[33] To compare our model results with those of previous studies, we first examine the dependence of the southward water flow leaving the Atlantic at 30°S on the amplitude of the SHW (Figure 5). An almost perfectly linear relationship is simulated for the setups with RBC (solid/dashed black lines). When MBC are applied instead of RBC (all other lines), circulation-salinity feedbacks are allowed to develop which tend to counteract the effect of the changes in wind forcing. The response of the Atlantic outflow to changes in the amplitude of SHW is thus largely damped in these setups (red, blue and green solid/dashed lines). However, NADW formation and Atlantic outflow shut down when weak winds are applied in the setups with low AMOC (red solid/dashed lines).

[34] These findings confirm previous studies [*Bugnion et al.*, 2006; *Rahmstorf and England*, 1997; *Toggweiler and Samuels*, 1995]. The tight coupling between SHW and the AMOC is an artifact of unrealistic restoring boundary conditions. We conclude furthermore that the strength of the coupling (i.e., the slope of the lines in Figure 5) significantly depends on the value of the diapycnal mixing parameter κ_{dia}. The setups with low κ_{dia} respond more sensitively to changes in wind forcing as compared to the setups with standard diapycnal diffusion.

[35] Figure 6 shows the strength of AMOC and deep SO overturning (below a depth of 1000 m) as a function of the scaling parameter ε. These quantities can be interpreted as the intensity of the northern and the southern circuit, respectively [*Toggweiler et al.*, 2006]. We analyze overturning in the deep SO as the interest here is on the link between the surface SO and the deep waters of the world ocean and not on shallow overturning.

[36] Across all the setups a significant trend is that the strength of AMOC (northern circuit) is positively correlated with the amplitude of the SHW. Modeled basin mean $\Delta^{14}C$ signatures in the Atlantic (not shown) reflect that the simulated changes in Atlantic ventilation are modulated by the changes in AMOC. This is no surprise since the Atlantic basin is mainly ventilated by NADW.

[37] In the SO the interplay between wind stress, overturning and ventilation seems less evident. There is a tendency, but no univocal trend, that the SHW strength controls the intensity of deep SO overturning (Figure 6b). The frequency and depth of convective events in the SO are clearly linked to the amplitude of SHW with stronger winds leading to more vigorous convection and vice versa (not shown). At the same time there is an evident correlation between basin mean $\Delta^{14}C$ signatures in the SO and the SHW strength (Figure 6c). The amplitude of ventilation changes in the SO also depends on the diapycnal mixing parameter κ_{dia} (Figure 6c).

[38] The clockwise overturning cell in the upper North Pacific is very sensitive to an intensification of the SHW. In all the model setups this cell considerably increases in strength and extent for strong winds which is manifest in the $\Delta^{14}C$ signature of the upper part of the Pacific basin (Figure 6d). Circulation-salinity feedbacks increase SSS in the North Pacific under MBC and amplify this sort of a response. In the case of weakened winds in contrast, the overturning cell becomes slower and shallower. A similar model response in the Pacific has also been found by *De Boer et al.* [2008], where an OGCM coupled to an energy moisture balance and a dynamic ice model is used to examine the circulation's sensitivity to changes in the amplitude of SH winds.

[39] The simulated $\Delta^{14}C$ signatures in the deep Pacific (Figure 6e) also indicate the tendency that the rate of ventilation increases for stronger SHW and decreases for weaker SHW. In some of the model setups, a stagnant water mass at the bottom of the Pacific basin appears when the

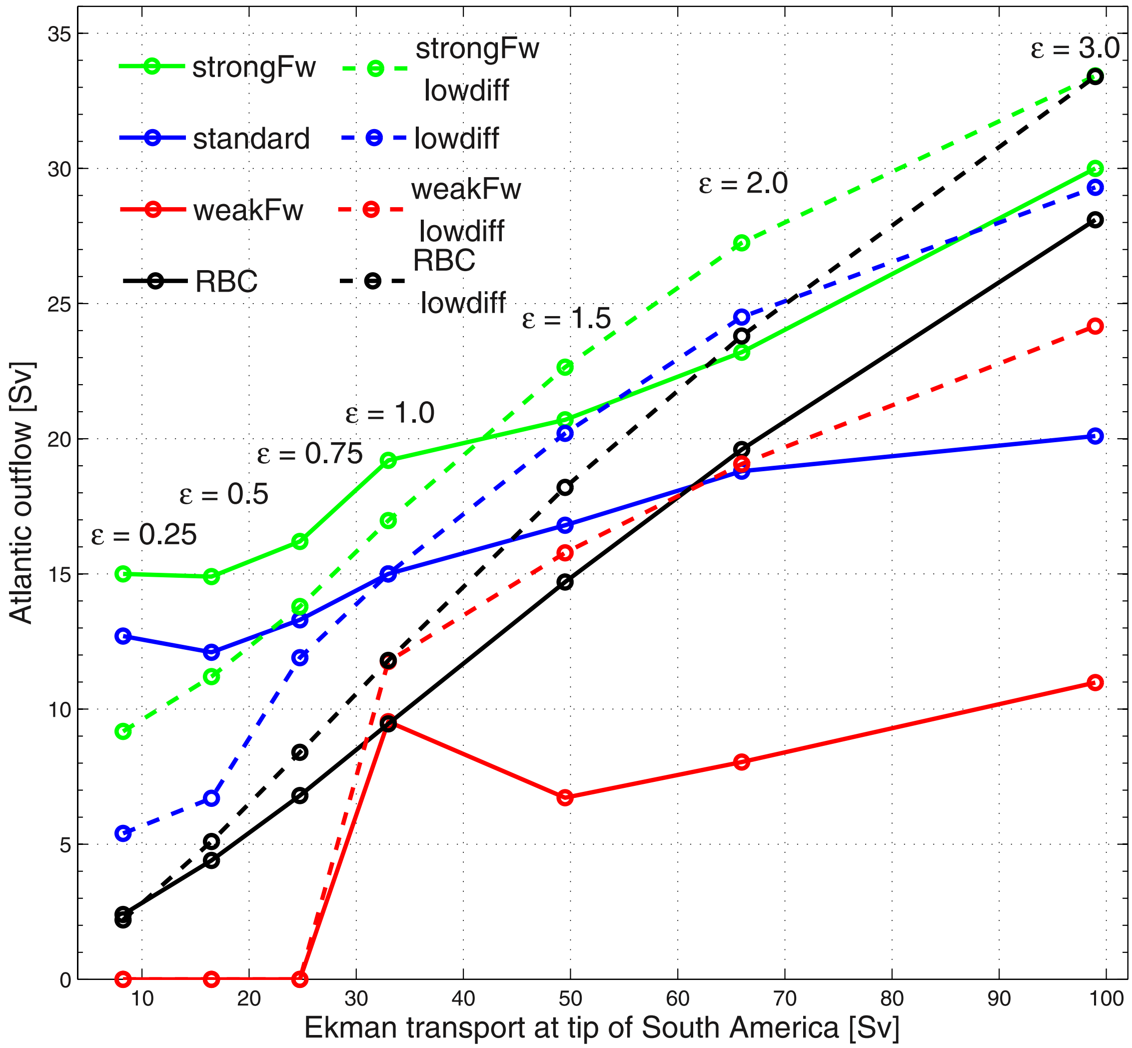

Figure 5. The "Drake Passage effect" [*Toggweiler and Samuels*, 1995]: The Atlantic outflow at the latitude of the Cape of Good Hope as a function of the northward Ekman transport at the tip of South America. With restoring boundary conditions (black lines) we model an almost perfectly linear relationship. When using mixed boundary conditions (green, blue, and red lines) we find a substantially weaker coupling between the Ekman transport and Atlantic outflow.

winds are weakened. In these cases, sharp drops in the deep Pacific $\Delta^{14}C$ signature are simulated (blue and green solid/dashed lines).

[40] In conclusion, these experiments cover a wide range with respect to SO circulation, convective activity and deep water ventilation and thus allow us to explore the carbon cycle response to a wide variety of physical changes.

3.1.2. Biogeochemistry and Atmospheric pCO_2

[41] Our results indicate that atmospheric CO_2 is rather sensitive to the amplitude of the SHW (Figure 7a). Intensified winds consistently induce a CO_2 rise in all the setups. The simulated changes are in the range of 35–60 ppm for a threefold strengthening (ε = 3.0). The biogeochemical rearrangements in response to a wind intensification are quite similar for all the setups. The modeled CO_2 rise in the atmosphere can be primarily attributed to an increase in sea surface pCO_2 in the SO.

[42] In the case of weakened winds however, the various setups respond differently. Setups with rather weak AMOC (black and red lines in Figure 7a) show a substantial drawdown in CO_2 of 30 to 55 ppm for a fourfold reduction in the strength of the SHW (ϵ = 0.25). The setups standard and strongFw, on the other hand, have very small responses of −2 to −7 ppm (blue and green solid lines). Finally, lowdiff and strongFw lowdiff display a nonmonotonic CO_2 response with respect to the wind-scaling factor ϵ (blue and green dashed lines). The modeled reorganizations of the DIC and alkalinity distributions as well as of sea surface pCO_2 reveal that qualitatively different biogeochemical responses occur when weak winds are imposed on the various model setups. The attribution of changes in CO_2 to individual mechanisms will be further explored in section 3.3.

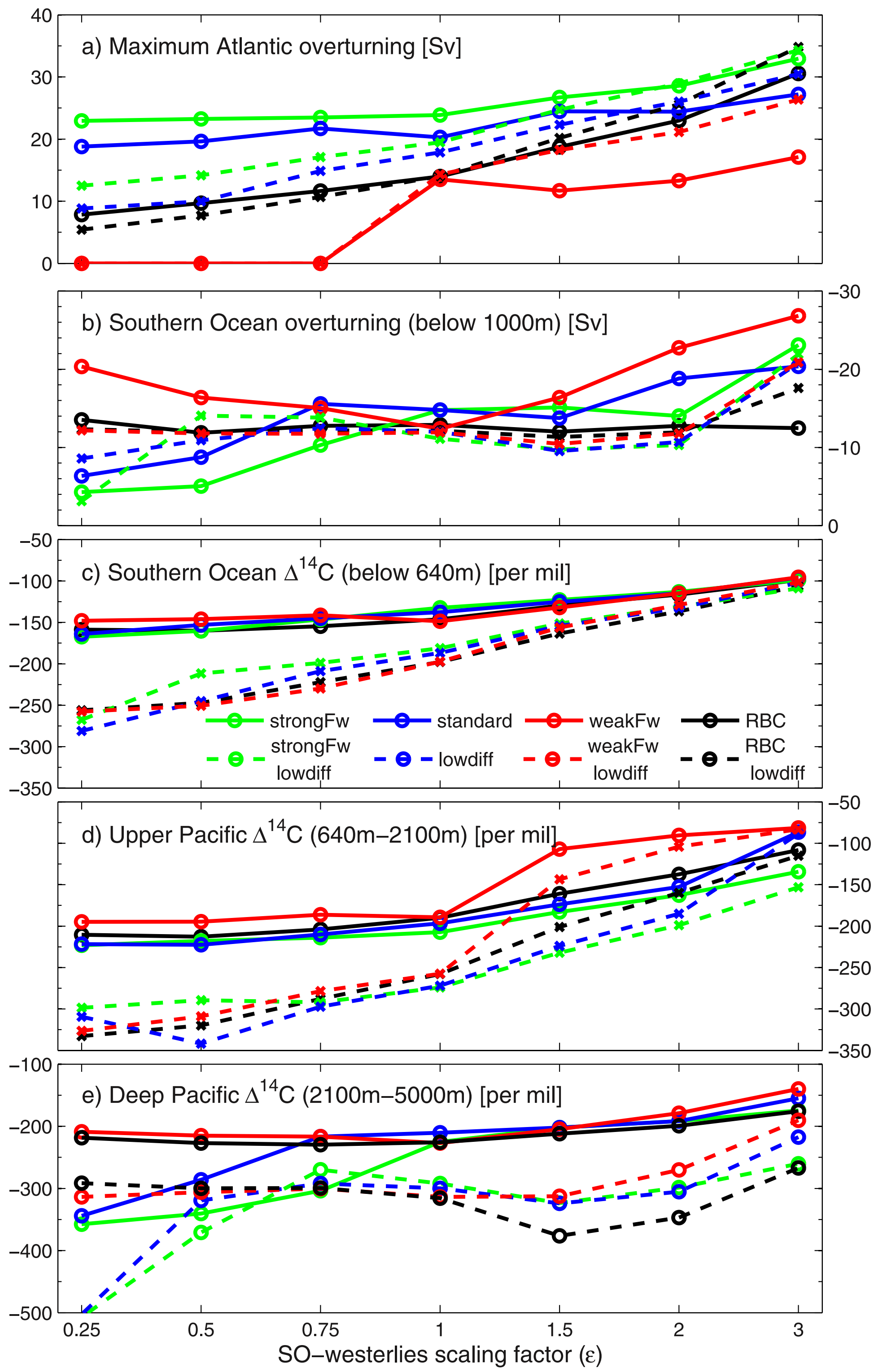

Figure 6. Circulation response to changes in SHW amplitude: (a) Maximum Atlantic overturning (Sv), (b) deep Southern Ocean overturning (Sv), (c) basin mean $\Delta^{14}C$ signatures (per mil) for the Southern Ocean (below 640 m), (d) the upper Pacific (640–2100 m), and (e) the deep Pacific (2100–5000 m) as a function of the scaling factor ε.

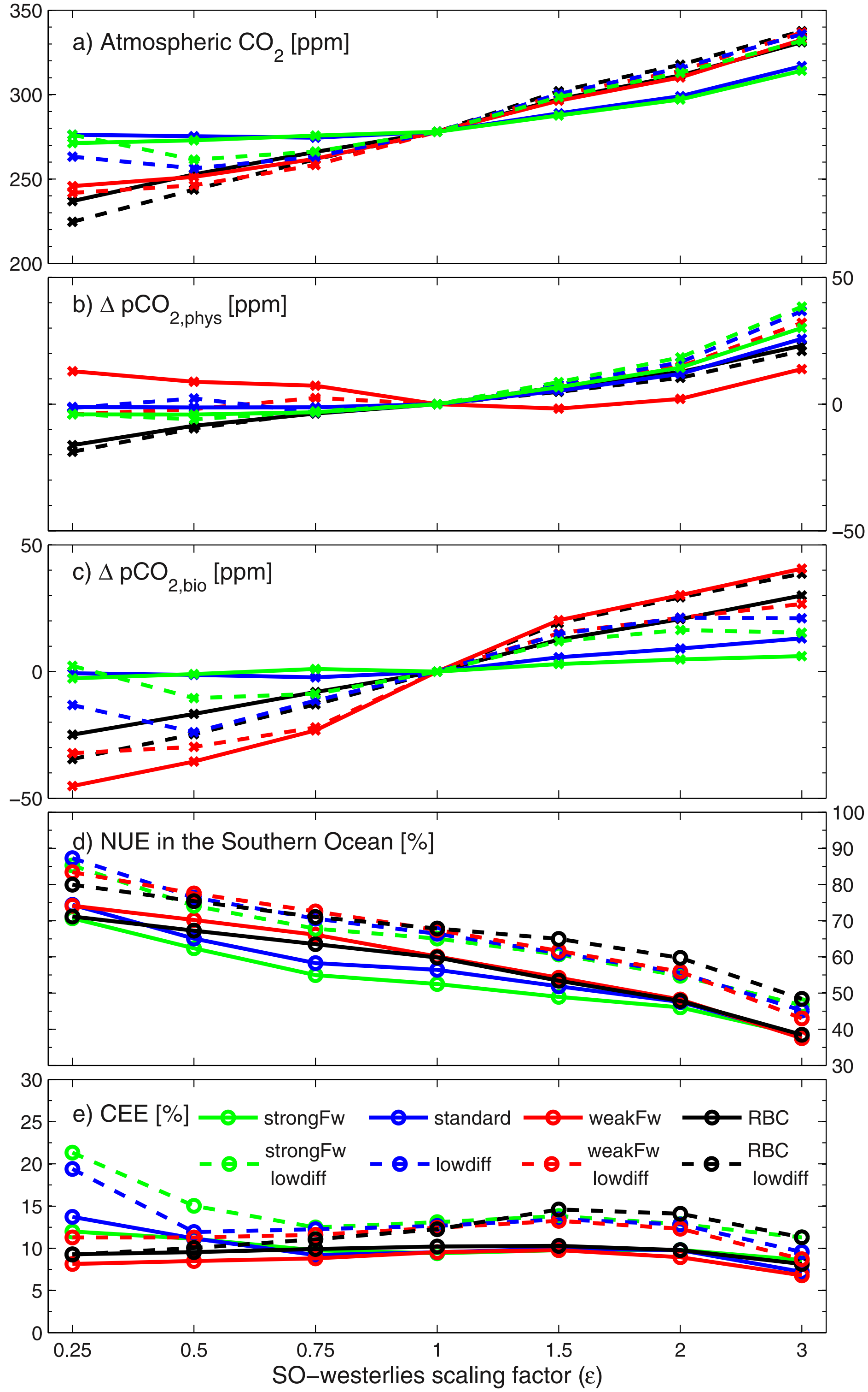

Figure 7. Biogeochemical response to changes in SHW amplitude: (a) Atmospheric CO_2 (ppm) and its variations split into (b) a physical and (c) a biological contribution as a function of the scaling factor ε. (d) Nutrient utilization efficiency in the Southern Ocean (%) (south of 34°S) and (e) the global $CaCO_3$ cycle efficiency (%).

3.2. Shift Experiments

3.2.1. Ocean Circulation and Ventilation

[43] Figure 8a shows that within the range of our shift scenarios for most setups we do not find any significant dependence of AMOC on the latitudinal position of the SHW. An exception to this are the two setups with MBC and weak AMOC (red dashed/solid lines). In both setups NADW formation collapses upon wind shifts in both directions.

[44] Equatorward shifts tend to reduce overturning in the SO whereas poleward shifts lead to an increase in SO overturning (Figure 8b). In the setups with MBC the typical structure of the deep SO overturning cell with a distinct maximum at around 40°S disappears when large equatorward shifts are applied. These results confirm the hypothesis that equatorward shifts tend to reduce the intensity of the southern overturning regime, as *Toggweiler et al.* [2006] suggested.

[45] However, the collapse of the SO overturning cell results in a decrease in SO ventilation only in the setups with low diapycnal diffusivity (Figure 8c). The corresponding setups show a decrease in $\Delta^{14}C$ of 50 to 77 per mil upon large equatorward shifts (red, blue and green dashed lines). In the other setups there is almost no change in SO ventilation when the SHW are shifted in position. Convective activity in the SO is rather unresponsive to shifts in wind stress for all the setups.

[46] As in the case of wind scaling, the Pacific circulation responds quite sensitively to latitudinal shifts in the SHW in all the setups. Equatorward displacements reduce the rate of upwelling from the deep to the surface and enhance the extent of the clockwise overturning cell in the upper North Pacific. The most prominent change caused by a poleward displacement is an increase in deep equatorial upwelling in the Pacific. However, the changes in deep Pacific overturning and deep Pacific ventilation are rather small (not shown).

3.2.2. Biogeochemistry and Atmospheric pCO_2

[47] The sensitivity of atmospheric CO_2 to latitudinal displacements of the zonal wind maximum is significantly smaller compared to its dependence on the amplitude of the SHW. The simulations indicate that poleward displacements of the winds induce a slight CO_2 drawdown whereas equatorward shifts tend to elevate atmospheric CO_2 (Figure 8d). The concentration does not drop below 260 ppm when poleward shifts are imposed. Upon equatorward displacements of up to 10° we simulate a maximum CO_2 concentration of 315 ppm. CO_2 in the RBC and RBC lowdiff cases responds the least to wind shifts (black lines in Figure 8d). The setups with rather strong AMOC (blue and green lines) also display a rather low sensitivity. Most responsive are weakFw and weakFw lowdiff (red lines), the only setups showing major circulation rearrangements upon wind shifts.

3.3. Decomposition of CO_2 Changes Into Physical and Biological Components

[48] To further understand the mechanisms controlling the CO_2 response, the simulated CO_2 changes are split into a "physical" and "biological" contribution as described below.

[49] Sinking organic particles transport carbon and nitrate to depth and thus deplete the sea surface in DIC while enriching it alkalinity. The organic matter cycle hence lowers sea surface pCO_2 and increases the ocean's carbon storage capacity compared to a world without marine biota. Nutrient utilization efficiency (NUE) is a frequently utilized measure to characterize the impact of the organic matter cycle on marine carbon cycling [*Sigman and Boyle*, 2000]:

$$NUE = \left(1 - \frac{\overline{[PO_4]}_{surface}}{\overline{[PO_4]}_{deep}}\right) \times 100 \qquad (2)$$

$\overline{[PO_4]}_{surface}$ and $\overline{[PO_4]}_{deep}$ are the average PO_4 concentrations in the surface and the deep ocean respectively.

[50] In contrast to the organic matter cycle, the production, sinking and redissolution of $CaCO_3$ shells act to deplete sea surface alkalinity and to increase sea surface pCO_2. To assess the effect of the $CaCO_3$ cycle on CO_2 partial pressures in the surface ocean we define similarly to NUE a $CaCO_3$ cycle efficiency (CCE):

$$CCE = \left(1 - \frac{\overline{[PAlk]}_{surface}}{\overline{[PAlk]}_{deep}}\right) \times 100 \qquad (3)$$

PAlk stands for potential alkalinity which is defined following *Brewer et al.* [1975]:

$$[PAlk] = [Alk] + \mathcal{R}_{N:P}[PO_4] \qquad (4)$$

[51] The second term on the right hand side of equation (4) represents a correction term to remove the influence of the organic matter cycle on the alkalinity distribution such that the distribution of PAlk is only affected by the cycling of biogenic $CaCO_3$.

[52] *Toggweiler et al.* [2006] restore surface PO_4 concentrations toward a fixed field to determine export production. However, reduced upwelling of remineralized carbon is accompanied by decreased nutrient supply to the surface and a likely change in NUE. Here, prognostic formulations of biological cycling are used (see auxiliary material) allowing surface nutrient fields and NUE to alter upon wind stress perturbations.

[53] The impact of changes in NUE and CEE on atmospheric CO_2 is quantified by an additional factorial run. Euphotic zone concentrations of PO_4 and potential alkalinity (PAlk) are instantaneously restored toward seasonally varying fields that were previously diagnosed in the initial steady state. In doing so, NUE and CEE remain largely unchanged. Note that equation (4) implies that this procedure also keeps sea surface alkalinities essentially unmodified when the model state is perturbed.

[54] Here, we arbitrarily term the modeled changes in atmospheric CO_2 resulting from the simulations with PO_4− and PAlk-restoring "physical" ($\Delta pCO_{2,phys}$). These are induced by changes in the interplay of circulation, CO_2 solubility and carbon chemistry, air-sea gas exchange, and

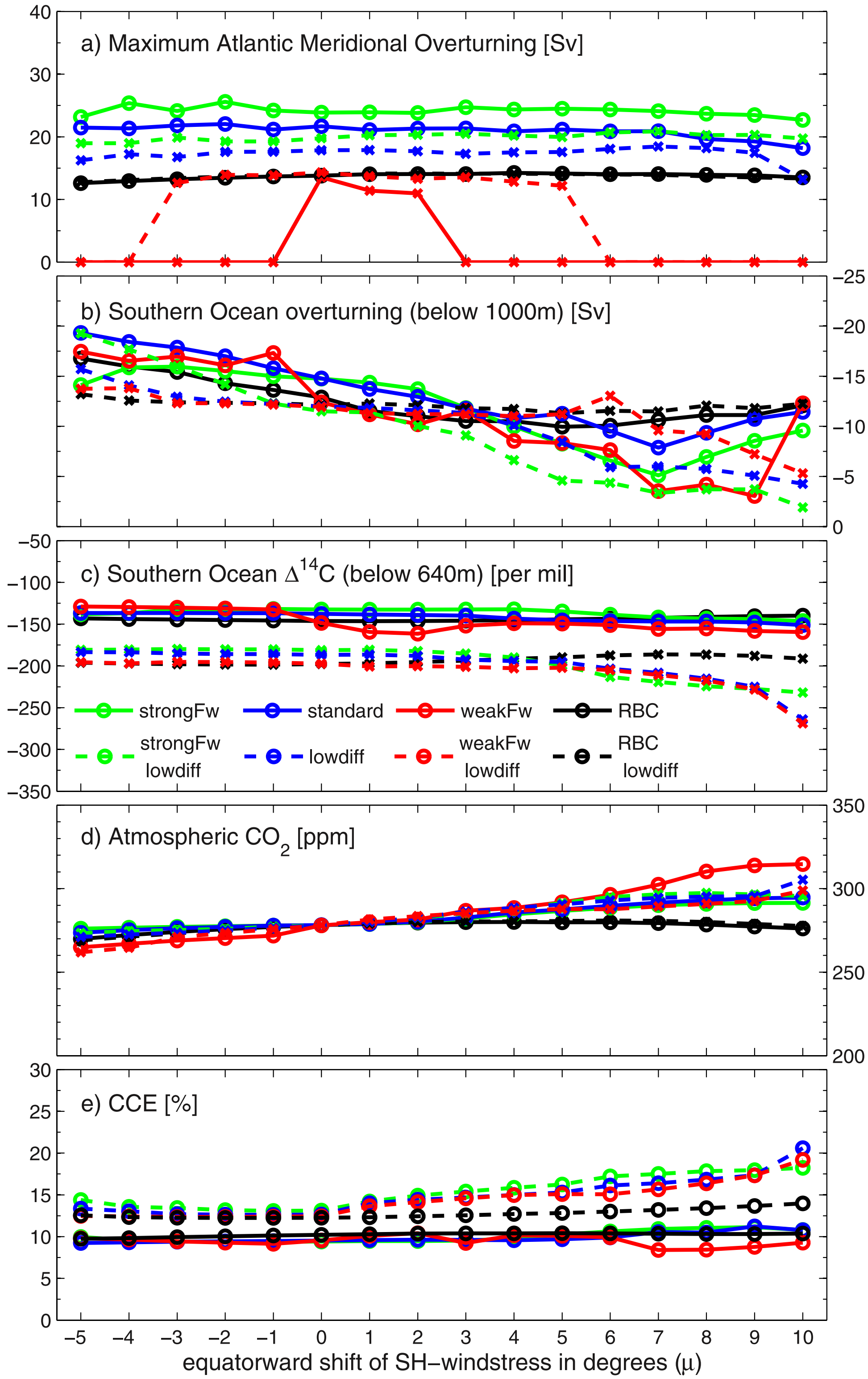

Figure 8. Model response to shifts in the latitudinal position of the SHW: (a) Maximum Atlantic overturning (Sv), (b) deep Southern Ocean overturning (Sv), (c) basin mean $\Delta^{14}C$ signature (per mil) in the Southern Ocean (below 640 m), (d) atmospheric CO_2 (ppm), and (e) the global $CaCO_3$ cycle efficiency (%) as a function of the shift parameter μ. Positive values of μ correspond to equatorward wind shifts, and negative values of μ relate to poleward wind shifts.

the cycling of organic material, calcite and silicic acid for maintained NUE and CEE.

[55] The difference in ΔpCO_2^{atm} between a nutrient restoring simulation ($\Delta\ pCO_{2,phys}$) and the corresponding run with fully prognostic biology is associated with $\Delta\ pCO_{2,bio}$ such that:

$$\Delta pCO_2^{atm}{}_{prognostic} = \Delta pCO_{2,phys} + \Delta pCO_{2,bio} \qquad (5)$$

$\Delta pCO_{2,bio}$ thus reflects CO_2 changes associated with altered NUE and CEE.

3.3.1. Scaling Experiments

[56] When the SHW are intensified physical and biological mechanisms play equally important roles in controlling CO_2 changes (Figures 7b and 7c). In the case of a threefold intensification (ε = 3.0) the physical component $\Delta pCO_{2,phys}$ explains 15 to 40 ppm of the CO_2 rise, largely because of altered circulation in the upper Pacific. A large fraction of this ocean region is ventilated by the clockwise overturning cell in the upper North Pacific when subjected to strong SHW (section 3.1.1). Cold and carbon-rich water masses stemming from the deep ocean get replaced by warm and well-ventilated waters that originate from the Pacific surface.

[57] $\Delta pCO_{2,bio}$ contributes 6 to 40 ppm to the modeled CO_2 increase in the case of very strong winds (ε = 3.0; Figure 7d). A decrease in NUE in the SO (south of 34°S) is mainly responsible. The rate of exchange between deep and surface waters in the SO increases and thus the supply of nutrients to the surface is enhanced which results in increased export production. Yet only a fraction of the increase in nutrient supply is utilized by marine biology and thus sea surface PO_4 and DIC concentrations rise. This implies that the marine organic matter cycle becomes less efficient in reducing sea surface pCO_2 when SHW are intensified. Changes in $CaCO_3$ cycle efficiency are small (Figure 7e) such that the overall biological response is dominated by the changes in the organic matter cycle which lead to an increase in atmospheric CO_2.

[58] As mentioned earlier (section 3.1.2), the various setups respond differently to weakened SHW. The simulations leading to a substantial CO_2 drawdown display a significant decrease of surface pCO_2 in the SO (RBC, RBC lowdiff, weakFw and weakFw lowdiff; black and red lines in Figure 7a). Such behavior is absent in the scenarios with a modest CO_2 response (standard, lowdiff, strongFw and strongFw lowdiff; blue and green lines in Figure 7a).

[59] Most setups display a very small physical CO_2 response when weak SHW are applied (Figure 7b). Only the RBC simulations (black lines) show a distinctly negative $\Delta pCO_{2,phys}$ of around -18 ppm for ϵ = 0.25. This CO_2 drawdown is associated with enhanced carbon storage in the upper Pacific and in the deep North Atlantic which results from a slowing and shoaling of the respective overturning cells.

[60] NUE in the SO increases monotonically in all the setups when the SHW are reduced in strength (Figure 7d). However, only in the setups RBC, RBC lowdiff, weakFw and weakFw lowdiff this NUE increase leads to a substantially negative $\Delta\ pCO_{2,bio}$ of 25 to 45 ppm for ϵ = 0.25 (black and red lines in Figure 7c). In the other setups (standard, lowdiff, strongFw and strongFw lowdiff) an increase in CEE counteracts the effect of enhanced NUE resulting in a modest $\Delta pCO_{2,bio}$ of -13 to +2 ppm when ϵ is set to 0.25 (blue and green lines in Figure 7c). In these simulations, stagnant water masses with low $\Delta^{14}C$ (blue and green lines in Figure 6e, section 3.1.1) emerge in the deep Pacific which induce major rearrangements in the cycling of DIC and alkalinity.

[61] In our model more than 85% of particulate organic matter is remineralized in the top 1000 meters, whereas about half of the $CaCO_3$ shells dissolve below a depth of 2500 m. For this reason, the $CaCO_3$ cycle is more strongly affected by the deep stagnant water masses than the organic matter cycle. The enhanced dissolution of $CaCO_3$ leads to an increase in alkalinity at depth and, as a consequence, to a depletion of alkalinity at the surface and in the thermocline, and thus to higher values of CEE when SHW are weakened (blue and green lines in Figure 7e). Low κ_{dia} leads to a more efficient alkalinity accumulation in the deep since upward diffusive transport is limited.

[62] In summary, an increase in SHW strength consistently leads to an increase in atmospheric CO_2 for all model setups in the range of 20 to 40 ppm per 100% change in wind stress strength. Decreased nutrient utilization efficiency and enhanced ventilation increase atmospheric CO_2 over the range of model setups. In contrast, the CO_2 response to weakened winds is sensitive to the model setup. Simulated changes are in the range of -2 to -55 ppm for a fourfold reduction in wind stress.

3.3.2. Shift Experiments

[63] The response in the carbon cycle to shifts in the position of the SHW is diverse for the different setups. The model setups with RBC show almost no sensitivity in atmospheric CO_2 when the SHW are shifted. In the setups with MBC, however, quite a robust trend emerges in the sense that poleward shifts induce a slight reduction in atmospheric CO_2 whereas equatorward shifts lead to a modest CO_2 increase (Figure 8d). Both physical and biological mechanisms contribute toward the simulated changes in atmospheric CO_2. $\Delta pCO_{2,phys}$ and $\Delta\ pCO_{2,bio}$ are generally of similar magnitude and of the same sign (not shown).

[64] The results show that the position of the Deacon cell [*Döös and Webb*, 1994] is tightly attached to the westerlies' zonal maximum. Equatorward wind shifts lead to northward shifts of this cell and of the associated fronts and hence increase the outcrop area. Accordingly, poleward displacements reduce the area where upwelled deep waters are exposed to the atmosphere. These circulation rearrangements in the SO are also manifest in modeled surface PO_4. The area of elevated PO_4 concentration in the SO decreases in the case of poleward wind shifts and increases for equatorward wind shifts.

[65] Preindustrial air-sea fluxes of CO_2 are characterized by outgassing in the SO (south of 44°S), uptake at midlatitudes of both hemispheres (18–44°S and 18–49°N) and strong outgassing in the tropics (18°N–18°S). This pattern is relatively well captured by means of inverse estimates in

Table 4. Additional Carbon Cycle Sensitivities[a]

Scenario	SH Westerlies ×0.5	CO_2 Solubility	Sea Ice Cover	$CaCO_3$ Compensation	500 GtC Terrestrial Input	Atmospheric CO_2 (ppm)	POM Export (GtC a^{-1})	$CaCO_3$ Export (GtC a^{-1})	NUE (%)	CEE (%)	Net $CaCO_3$ Flux From Sediments (GtC)
control						278	10.96	0.98	79.4	12.69	-
Exp1	x					256	7.54	0.68	84.6	12.68	-
Exp2	x	x				232	7.66	0.69	84.3	12.51	-
Exp3	x		x			261	7.62	0.68	84.4	12.65	-
Exp4	x			x		253	7.62	0.68	84.4	-	74
Exp5	x				x	294	7.56	0.68	84.6	12.68	-
Exp6	x	x	x	x	x	256	7.69	0.69	84.4	-	284
Exp7	x	x	x	x		233	7.62	0.68	84.4	-	87

[a]The mechanisms considered in the different simulations are listed along with the results obtained at steady state.

a number of ocean models including the Bern3D model [*Mikaloff Fletcher et al.*, 2007]. In the wind shift experiments the most prominent changes in sea surface pCO_2 occur in a latitudinal belt at around 40°S, the location of the northern edge of the modern Deacon cell. Shifts toward the equator elevate pCO_2 and displacements toward the pole lead to a pCO_2 reduction in that region. The model results thus suggest that the zone of CO_2 outgassing in the SO contracts upon poleward wind shifts and expands upon equatorward shifts, explaining the simulated changes in $\Delta pCO_{2,phys}$.

[66] The biological contribution $\Delta pCO_{2,bio}$ is dominated by NUE changes in the setups with standard diapycnal diffusivity κ_{dia} and by CEE changes in the setups with low κ_{dia}. In the former an increase in the Deacon overturning under equatorward shifts increases both nutrient supply and export production in the SO by about 20%. The result is a slight reduction in NUE in the SO (not shown). In the latter reduced SO ventilation and decreased deep upwelling in the Pacific enhance CEE when the SHW are shifted toward the equator (Figure 8e).

3.4. Additional Model Sensitivities

[67] To examine further model sensitivities, in addition to halving the SH westerlies' amplitude, we separately apply to the setup lowdiff the effects of (1) increased glacial CO_2 solubility resulting from changes in SST and SSS, (2) hampered air-sea gas exchange in the SO due to enhanced sea ice cover, (3) $CaCO_3$ compensation, and (4) a 500 GtC carbon input into the atmosphere stemming from the terrestrial biosphere [e.g., *Shackleton*, 1977] (Table 4, Exp2, Exp3, Exp4 and Exp5; for details of these simulations see auxiliary material). Finally, we take into account all of these mechanisms simultaneously (Table 4: Exp6). Table 4 summarizes the simulations and the results. The changes in the DIC distribution due to a halving of the SHW (Exp1-control) are illustrated in Figures 9a and 9b, the DIC changes in response to the additional processes (Exp6-Exp1) are depicted in Figures 9c and 9d.

[68] When the four additional effects are taken into account simultaneously (Exp6) we achieve a total CO_2 drawdown of 22 ppm to 256 ppm. Increased biological efficiencies ($\Delta pCO_{2,bio}$ = −24 ppm), enhanced CO_2 solubility (−24 ppm) and $CaCO_3$ compensation (−15 ppm) are mainly responsible for the CO_2 reduction. On the other hand, the terrestrial carbon input (+38 ppm, without $CaCO_3$ compensation), physical rearrangements ($\Delta pCO_{2,phys}$ = +2 ppm) and hampered gas exchange in the SO due to extended sea ice coverage (+5 ppm) elevate CO_2.

[69] The halving of the SH westerly winds' amplitude induces an AMOC reduction of about 8 Sv and deteriorates the ventilation in the upper Pacific and the Southern Ocean (blue dashed lines in Figures 6a, 6c, and 6d for ϵ = 0.5). Reduced nutrient supply to the surface decreases POM export production by about 30%, but increases global NUE by 5% (Table 4). Export of biogenic $CaCO_3$ also decreases, but CEE remains virtually unchanged. The induced changes in marine carbon cycling lead to a drawdown of 22 ppm (Exp1). In this simulation, deep ocean alkalinity and DIC increase roughly in concert such that their difference, which approximates the CO_3^{2-} concentration, changes only marginally. For this reason, we simulate only a small additional response of −3 ppm when $CaCO_3$ compensation is considered in addition to the halving of the SHW (Exp4).

[70] The modeled drawdown of 24 ppm due to the solubility effect (Exp2) is very close in magnitude to the estimate of 23.5 ppm given by *Sigman and Boyle* [2000] which was calculated using the CYCLOPS ocean box model [*Keir*, 1988] and a rough guess of glacial SST and SSS. As found in other GCMs [*Archer et al.*, 2003], increased sea ice cover in the SO leads to higher atmospheric CO_2 (Exp3). Enhanced sea ice cover excludes surface waters with low pCO_2 from gas exchange such that the new atmospheric CO_2 equilibrium is shifted toward a higher pCO_2. The input of 500 GtC carbon into the atmosphere induces a CO_2 increase of 38 ppm without $CaCO_3$ compensation and 23 ppm with it. The first value is in good agreement with an estimate of 37 ppm for the uncompensated case [*Archer et al.*, 2000a], the latter is somewhat higher than the 17 ppm estimate reported in that same paper for the compensated case.

[71] In a further experiment (Exp7), all of the additional effects described above were considered, but the terrestrial carbon input was excluded. In this case CO_2 was 233 ppm. The total simulated 45 ppm drawdown is of similar magnitude as the 43 ppm reduction modeled by *Brovkin et al.* [2007] in a comparable model configuration. In their study glacial SST, SSS, ocean circulation and sea ice cover were obtained by prescribing a complete set of glacial forcings to the CLIMBER-2 intermediate complexity Earth system model.

[72] Changes in oceanic DIC concentrations resulting from the wind weakening and associated changes in biological efficiencies (Figures 9a and 9b) are relatively large

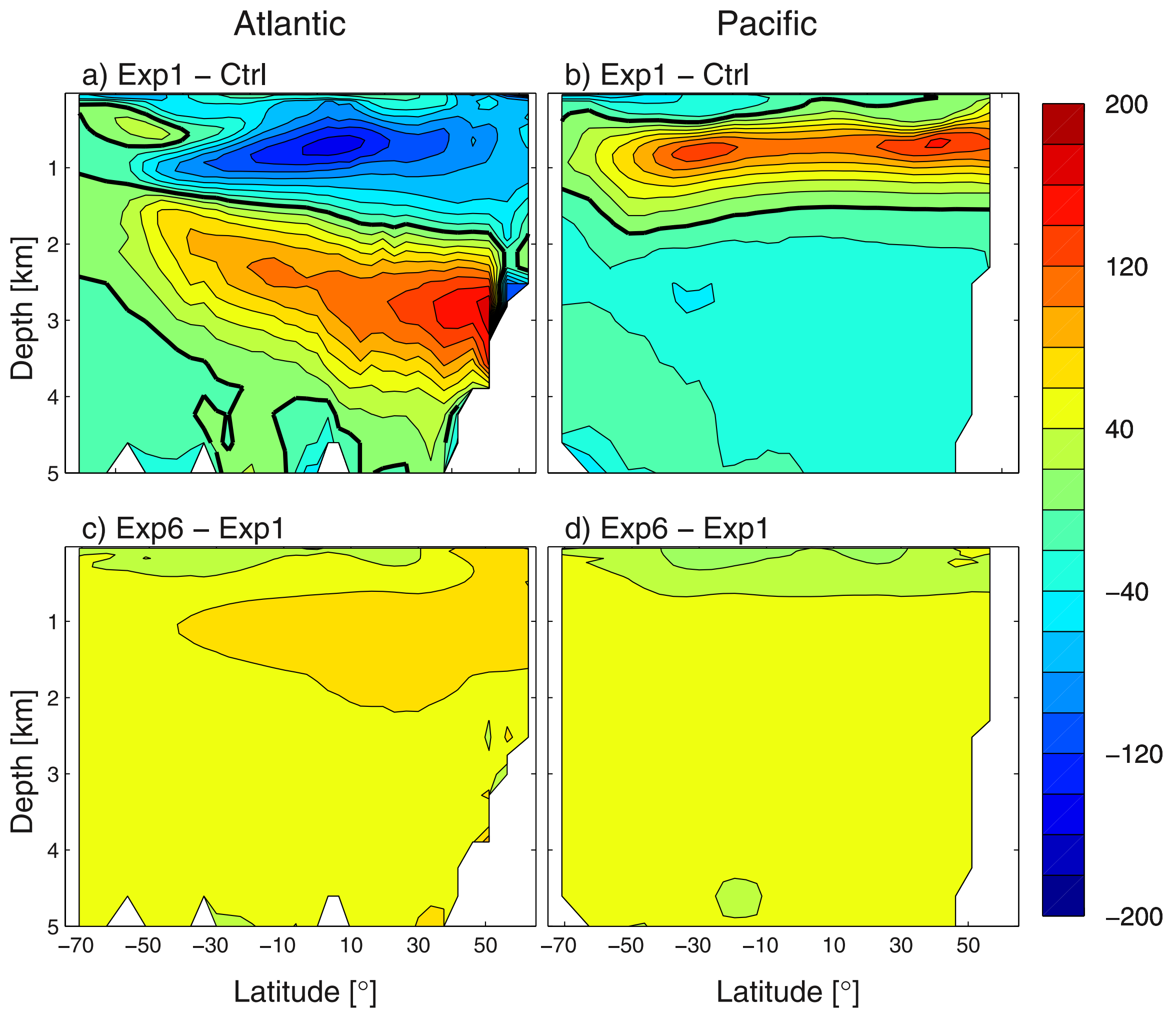

Figure 9. Changes in zonal mean DIC (μmol kg^{-1}) (a and b) due to a halving of the SHW amplitude and (c and d) in response to modified CO_2 solubility, sea ice cover, $CaCO_3$ compensation, and a 500 GtC carbon input into the atmosphere. Zero lines are shown as thick black contours.

and spatially heterogeneous. The concentrations increase in the upper Pacific and in the Atlantic at intermediate depths (2–3 km). In the intermediate and deep Pacific, as well as in the upper Atlantic, carbon storage is reduced. Changes in the DIC distribution induced by increased solubility, enhanced SO sea ice cover, $CaCO_3$ compensation and a 500 GtC carbon input into the atmosphere are generally higher in the ocean interior than near the surface (Figures 9c and 9d). Most of the additional carbon that is taken up by the ocean in response to these four mechanisms is transported by NADW.

4. Summary and Conclusions

[73] The focus of this study is a hypothesis that calls for reduced upwelling of CO_2-rich deep waters in the SO resulting from an equatorward shift of the SHW to explain low glacial CO_2 levels in the atmosphere [*Toggweiler et al.*, 2006]. We perform a systematic sensitivity analysis of the large-scale ocean circulation, marine carbon cycling and atmospheric CO_2 to changes in the strength and position of the SHW to probe this mechanism in the Bern3D coarse-resolution ocean model.

[74] Mechanisms of CO_2 variations are quantified by targeted sensitivity simulations and analyses. The wide range of model setups and wind stress scenarios applied resulted in a variety of simulated physical and biogeochemical responses. These include strongly reduced deep SO overturning and low ventilation of the deep ocean, corresponding to the weak southern circuit suggested by *Toggweiler et al.* [2006]. The results, in combination with available evidence on glacial winds, suggest that SH wind changes played a limited role in modulating glacial-interglacial atmospheric CO_2 concentrations. In addition, and in further conflict with *Toggweiler et al.* [2006], an equatorward shift in SHW results in a CO_2 increase and not in the hypothesized decrease.

[75] The Bern3D model is able to adequately represent ocean circulation and the cycling of major biogeochemical tracers (see section 2.2). Yet, as with any modeling study, a number of caveats apply to our results. Although the preindustrial distribution of DIC is reasonably simulated

compared to data-based estimates (see Figure 1c and Table 3), there remains some uncertainty related to the role of gas exchange and the solubility pump (see section 2.2). Instead by an interactive atmosphere, SST and SSS are constrained by applying restoring or mixed boundary conditions. However, our results are in good agreement with a recent study by *De Boer et al.* [2008] who examine the response of the meridional overturning circulation to changes in the SHW strength using an OGCM coupled to an energy moisture balance model for the atmosphere. Furthermore, the authors emphasize the important role of winds in stirring salinity gradients in the ocean. In our study, salinity-circulation feedbacks are accounted for under changes in wind stress when mixed boundary conditions are applied.

[76] Eddy fluxes are believed to play a more central role in the dynamics of the SO than in other areas of the world ocean [*Rintoul et al.*, 2001]. Eddies are not represented explicitly in the Bern3D model. Furthermore, ocean-ice interactions in the SO are thought to be crucial for the formation of deep waters around Antarctica and convection is only represented in a highly parameterized way.

[77] A reduction in the strength of SHW leads to a decline in simulated atmospheric CO_2. Ventilation in the SO is reduced by a decrease in the frequency and depth of convective events. In addition, biological mechanisms contribute toward the modeled CO_2 drawdown which is up to 34 ppm for a 50% reduction in SHW strength. A 50% increase on the other hand leads to a rise in atmospheric CO_2 of up to 24 ppm.

[78] When the SHW are shifted in their latitudinal position the meridional overturning circulation, marine carbon cycling and atmospheric CO_2 respond relatively insensitively. A poleward shift of 5° lowers CO_2 by up to 16 ppm whereas an equatorward shift of 5° induces a CO_2 increase of maximum 14 ppm. The wind shifts do not substantially alter ventilation in the SO. Rather they affect atmospheric CO_2 by changing the outcrop area of deep waters. As in the wind-scaling simulations changes in marine biology tend to enforce the CO_2 response that is induced by physical mechanisms.

[79] In additional sensitivity runs, a limited set of mechanisms for low CO_2 is quantified. We model a drawdown of atmospheric CO_2 to 256 ppm from a preindustrial value of 278 ppm when prescribing reduced wind stress in the SO, enhanced CO_2 solubility, reduced gas transfer velocities by sea ice expansion and a 500 GtC carbon input into the atmosphere due to reduced terrestrial carbon storage in glacial times. An increase in biological efficiencies (−24 ppm) and the enhanced CO_2 solubility (−24 ppm) are mainly responsible for the CO_2 reduction. $CaCO_3$ compensation in response to reduced wind stress alone is small (−3 ppm). However, the reaction of $CaCO_3$ sediments reduces the atmospheric CO_2 rise due to the 500 GtC carbon input from 38 ppm to 23 ppm. The simulated amplitudes of the additional effects are generally in good agreement with those reported in previous studies [e.g., *Brovkin et al.*, 2007; *Archer et al.*, 2000a; *Sigman and Boyle*, 2000]. Additional mechanisms than the limited set considered here are required to account for the full glacial-interglacial CO_2 change [see, e.g., *Broecker and Henderson*, 1998; *Sigman and Boyle*, 2000; *Archer et al.*, 2000a; *Kohfeld et al.*, 2005].

[80] Physical as well as biological oceanic controls on CO_2 should be taken into account simultaneously in scenarios of low glacial atmospheric CO_2. Decreased ventilation in the SO reduces the supply of nutrient-rich deep waters to the surface potentially increasing the efficiency of the organic matter cycle in drawing down surface pCO_2. In contrast, a reduction in deep ocean ventilation might also lead to a substantial increase of deep ocean alkalinity in response to a more efficient $CaCO_3$ cycle. This would reduce surface alkalinity and hence increase surface pCO2. These effects of the organic matter and $CaCO_3$ cycle are antipodal with respect to atmospheric CO_2 and their respective amplitudes depend on the details of the glacial circulation. We have assessed these biological implications on atmospheric CO_2 using the concepts of nutrient utilization efficiency (NUE) and $CaCO_3$ cycle efficiency (CCE).

[81] The idea of changes in deep ocean ventilation as being an important reason for increased CO_2 storage in the glacial ocean [*Toggweiler*, 1999] appears tempting given the available data [e.g., *Duplessy et al.*, 1988; *Adkins et al.*, 2002; *Hodell et al.*, 2003; *Marchitto et al.*, 2007]. However, our results indicate that mechanisms other than wind changes were probably more relevant for altering the ventilation of the ocean's deep layers. For instance, *Watson and Naveira Garabato* [2006] propose that mixing in the SO was slower because denser deep waters were formed and a decreased buoyancy flux at the surface suppressed upwelling. *Sigman et al.* [2004] suggest that the cooling caused increased stratification by weakening the role of temperature in polar ocean density structure. If variations in the SHW are invoked as the main mechanism for the glacial CO_2 drawdown a reduction in SHW strength of at least 50% would be required. Such a weakening in SO winds appears rather unlikely given the available reconstructions discussed in section 2.3 [e.g., *Shulmeister et al.*, 2004; *Otto-Bliesner et al.*, 2006; *Rojas et al.*, 2008]. These conclusions are supported by a recent study that is based on the LOVECLIM earth system model of intermediate complexity [*Menviel et al.*, 2008].

[82] **Acknowledgments.** This study was funded by the Swiss National Science Foundation and the EU projects CARBOOCEAN (511176-2) and EUROCEANS (511106-2). P.P. acknowledges support from the Marie Curie International Incoming Fellowship. We thank N. R. Edwards, S. A. Müller, and T. F. Stocker for helpful comments. Critical reviews from V. Brovkin, J. R. Toggweiler, and one anonymous reviewer are acknowledged.

References

Adkins, J. F., K. McIntyre, and D. P. Schrag (2002), The salinity, temperature and $\delta^{18}O$ content of the glacial deep ocean, *Science*, *298*, 1769–1773.

Anderson, L., and J. Sarmiento (1994), Redfield ratios of remineralization determined by nutrient data analysis, *Global Biogeochem. Cycles*, *8*, 65–80.

Archer, D., A. Winguth, D. Lea, and N. Mahowald (2000a), What caused the glacial/interglacial atmospheric pCO_2 cycles?, *Rev. Geophys.*, *38*, 159–189.

Archer, D., G. Eshel, A. Winguth, W. Broecker, R. Pierrehumbert, M. Tobis, and R. Jacob (2000b), Atmospheric pCO_2 sensitivity to the biological pump of the ocean, *Global Biogeochem. Cycles*, *14*, 1219–1230.

Archer, D. E., P. A. Martin, J. Milovich, V. Brovkin, G.-K. Plattner, and C. Ashendel (2003), Model sensitivity in the effect of Antarctic sea ice and stratification on atmospheric pCO_2, *Paleoceanography*, *18*(1), 1012, doi:10.1029/2002PA000760.

Aumont, O., and L. Bopp (2006), Globalizing results from ocean in situ iron fertilization studies, *Global Biogeochem. Cycles*, *20*, GB2017, doi:10.1029/2005GB002591.

Brewer, P. G., G. T. F. Wong, M. P. Bacon, and D. W. Spencer (1975), An oceanic calcium problem?, *Earth Planet. Sci. Lett.*, *26*, 81–87.

Broecker, W. S., and G. M. Henderson (1998), The sequence of events surrounding Termination II and their implications for the cause of glacial-interglacial CO_2 changes, *Paleoceanography*, *13*, 352–364.

Broecker, W., J. Lynch-Stieglitz, D. Archer, M. Hoffmann, E. Maier-Reimer, O. Marchal, T. Stocker, and N. Gruber (1999), How strong is the Harvadton-Bear constraint?, *Global Biogeochem. Cycles*, *13*, 817–820.

Brovkin, V., A. Ganopolski, D. Archer, and S. Rahmstorf (2007), Lowering of glacial atmospheric CO_2 in response to changes in oceanic circulation and marine biogeochemistry, *Paleoceanography*, *22*, PA4202, doi:10.1029/2006PA001380.

Bryan, F. (1986), High-latitude salinity effects and interhemispheric thermohaline circulations, *Nature*, *323*, 301–304.

Bugnion, V., C. Hill, and P. H. Stone (2006), An adjoint analysis of the meridional overturning circulation in a hybrid coupled model, *J. Clim.*, *19*, 3751–3767.

Conkright, M. E., and T. P. Boyer (2002), World Ocean Atlas 2001: Objective analyses, data statistics, and figures, CD-ROM documentation, 17 pp., Natl. Oceanogr. Data Cent., Silver Spring, Md.

Conkright, M., H. E. Garcia, T. D. O'Brien, R. A. Locarnini, T. P. Boyer, C. Stephens, and J. I. Antonov (2002), *World Ocean Atlas 2001*, vol. 4, *Nutrients, NOAA Atlas NESDIS*, vol. 52, NOAA, Silver Spring, Md.

De Boer, A. M., J. R. Toggweiler, and D. M. Sigman (2008), Atlantic dominance of the meridional overturning circulation, *J. Phys. Oceanogr.*, *38*, 435–450.

Döös, K., and D. J. Webb (1994), The Deacon Cell and the other meridional overturning cells in the Southern Ocean, *J. Phys. Oceanogr.*, *24*, 429–442.

Duplessy, J. C., N. J. Shackleton, R. G. Fairbanks, L. Labeyrie, D. Oppo, and N. Kallel (1988), Deepwater source variations during the last climatic cycle and their impact on the global deepwater circulation, *Paleoceanography*, *3*, 343–360.

Edwards, N. R., and R. Marsh (2005), Uncertainties due to transport-parameter sensitivity in an efficient 3-D ocean-climate model, *Clim. Dyn.*, *3*, 67–94.

Falkowski, P. G., R. T. Barber, and V. Smetacek (1998), Biogeochemical controls and feedbacks on ocean primary productivity, *Science*, *281*, 200–206.

Gillett, N., and D. Thompson (2003), Simulation of recent Southern Hemisphere climate change, *Science*, *302*, 273–275.

Griffies, S. M. (1998), The Gent-McWilliams skew flux, *J. Phys. Oceanogr.*, *28*, 831–841.

Gruber, N., and J. Sarmiento (2002), Large-scale biogeochemical interactions in elemental cycles, in *The Sea*, pp. 337–399, John Wiley, New York.

Hall, A., and M. Visbeck (2002), Synchronous variability in the Southern Hemisphere atmosphere, sea ice, and ocean resulting from the Annular Mode, *J. Clim.*, *15*, 3043–3057.

Harrison, S., and J. Dodson (1993), Climates of Australia and New Guinea since 18000 years, in *Global Climates Since the Last Glacial Maximum*, edited by H. E. Wright Jr. et al., pp. 265–293, Univ. of Minn. Press, Minneapolis.

Heinze, C., E. Maier-Reimer, A. M. E. Winguth, and D. Archer (1999), A global oceanic sediment model for long-term climate studies, *Global Biogeochem. Cycles*, *13*, 221–250.

Heusser, C. (1989), Southern westerlies during the Last Glacial Maximum, *Quat. Sci. Rev.*, *31*, 423–425.

Hodell, D. A., K. A. Venz, C. D. Charles, and U. S. Ninnemann (2002), Pleistocene vertical carbon isotope and carbonate gradients in the South Atlantic sector of the Southern Ocean, *Geochem. Geophys. Geosyst.*, *4*(1), 1004, doi:10.1029/2002GC000367.

Iglesias-Rogdríguez, M. D., R. Armstrong, R. A. Feely, R. Hood, J. Kleypass, J. D. Milliman, C. L. Sabine, and J. L. Sarmiento (2002), Progress made in the study of the ocean's carbon budget, *Eos Trans. AGU*, *83*, 374–375.

Kalnay, E., et al. (1996), The NCEP/NCAR 40-year reanalysis project, *Bull. Am. Meteorol. Soc.*, *77*, 437–471.

Keir, R. S. (1988), On the late Pleistocene ocean geochemistry and circulation, *Paleoceanography*, *3*, 413–445.

Key, R. M., et al. (2004), A global ocean carbon climatology: Results from global data analysis project (GLODAP), *Global Biogeochem. Cycles*, *18*, GB4031, doi:10.1029/2004GB002247.

Kim, S.-J., G. M. Flato, and G. J. Boer (2002), A coupled climate model simulation of the Last Glacial Maximum, part2: Approach to equilibrium, *Clim. Dyn.*, *20*, 635–661.

Kohfeld, K. E., C. Le Quéré, R. Anderson, and S. Harrison (2005), Role of marine biology in glacial-interglacial CO_2 cycles, *Science*, *308*, 74–78.

Kuhlbrodt, T., A. Griesel, M. Montoya, A. Levermann, M. Hofmann, and S. Rahmstorf (2007), On the driving processes of the Atlantic meridional overturning circulation, *Rev. Geophys.*, *45*, RG2001, doi:10.1029/2004RG000166.

Le Quéré, C., et al. (2007), Saturation of the Southern Ocean CO_2 sink due to recent climate change, *Science*, *316*, 1735–1738.

Levitus, S., and T. Boyer (1994), *World Ocean Atlas 1994*, vol. 4, *Temperature, NOAA Atlas NESDIS 4*, 117 pp., NOAA, Silver Spring, Md.

Levitus, S., R. Burgett, and T. Boyer (1994), *World Ocean Atlas 1994*, vol. 3, *Salinity, NOAA Atlas NESDIS 3*, 99 pp., NOAA, Silver Spring, Md.

Lovenduski, N. S., and N. Gruber (2005), Impact of the Southern Annular Mode on Southern Ocean circulation and biology, *Geophys. Res. Lett.*, *32*, L11603, doi:10.1029/2005GL022727.

Lovenduski, N. S., N. Gruber, S. C. Doney, and I. D. Lima (2007), Enhanced CO_2 outgassing in the Southern Ocean from a positive phase of the Southern Annular Mode, *Global Biogeochem. Cycles*, *21*, GB2026, doi:10.1029/2006GB002900.

Marchitto, T. M., S. J. Lehman, J. D. Ortiz, J. Flückiger, and A. van Geen (2007), Marine radiocarbon evidence for the mechanism of deglacial atmospheric CO_2 rise, *Science*, *316*, 1456–1459.

Markgraf, V. (1989), Reply to C. J. Heusser's "Southern westerlies during the Last Glacial Maximum,", *Quat. Sci. Rev.*, *31*, 426–432.

Menviel, L., A. Timmermann, A. Mouchet, and O. Timm (2008), Climate and marine carbon cycle response to changes in the strength of the Southern Hemispheric westerlies, *Paleoceanography*, *23*, PA4201, doi:10.1029/2008PA001604.

Mikaloff Fletcher, S. E., et al. (2007), Inverse estimates of the oceanic sources and sinks of natural CO_2 and the implied oceanic carbon transport, *Global Biogeochem. Cycles*, *21*, GB1010, doi:10.1029/2006GB002751.

Moreno, P., T. Lowell, G. L. Jacobson Jr., and G. Denton (1999), Abrupt vegetation and climate changes during the Last Glacial Maximum and last termination in the Chilean lake district: A case study from Canal de la Puntilla (41°S), *Geogr. Ann., Ser. A, Phys. Geogr.*, *81*(2), 285–311, doi:10.1111/1468-0459.00059.

Müller, S. A., F. Joos, N. R. Edwards, and T. F. Stocker (2006), Water mass distribution and ventilation time scales in a cost-efficient, three-dimensional ocean model, *J. Clim.*, *19*, 5479–5499.

Müller, S. A., F. Joos, G.-K. Plattner, N. R. Edwards, and T. F. Stocker (2008), Modeled natural and excess radiocarbon: Sensitivities to the gas exchange formulation and ocean transport strength, *Global Biogeochem. Cycles*, *22*, GB3011, doi:10.1029/2007GB003065.

Najjar, R. G., and J. Orr (1999), Biotic-HOWTO, technical report, 15 pp., Lab. des Sci. du Clim. et l'Environ., Comm. à l'Energie At. Saclay, Gif-sur-Yvette, France. (Available at http://www.ipsl.jussieu.fr/OCMIP/phase2/simulations/Biotic/HOWTO-Biotic.html).

Orr, J., R. G. Najjar, C. L. Sabine, and F. Joos (1999), Abiotic-HOWTO, technical report, 25 pp., Lab. des Sci. du Clim. et l'Environ., Comm. à l'Energie At. Saclay, Gif-sur-Yvette, France. (Available at http://www.ipsl.jussieu.fr/OCMIP/phase2/simulations/Abiotic/HOWTO-Abiotic.html).

Otto-Bliesner, B. L., E. C. Brady, G. Clauzet, R. Tomas, S. Levis, and Z. Kothavala (2006), Last Glacial Maximum and Holocene climate in CCSM3, *J. Clim.*, *19*, 2526–2544.

Parekh, P., F. Joos, and S. A. Müller (2008), The role of aeolian iron flux in controlling carbon dioxide fluctuations during Antarctic warm events, *Paleoceanography*, *23*, PA4202, doi:10.1029/2007PA001531.

Paul, A., and C. Schäfer-Neth (2003), Modeling the water masses of the Atlantic Ocean at the Last Glacial Maximum, *Paleoceanography*, *18*(3), 1058, doi:10.1029/2002PA000783.

Rahmstorf, S., and M. England (1997), Influence of Southern Hemisphere winds on North Atlantic deep water flow, *J. Phys. Oceanogr.*, *27*, 2040–2054.

Rintoul, S. R., C. W. Hughes, and D. Olberts (2001), The Antarctic circumpolar current system, in *Ocean Circulation and Climate*, pp. 271–302, Academic, San Diego, Calif.

Rojas, M., P. Moreno, M. Kageyama, M. Crucifix, C. Hewitt, A. Abe-Ouchi, R. Ohgaito, E. C. Brady, and P. Hope (2006), The Southern Westerlies during the last glacial maximum in PMIP2 simulations, *Clim. Dyn*, doi:10.1007/s00382-008-0421-7, in press.

Russell, J., K. Dixon, A. Gnanadesikan, R. Stouffer, and J. Toggweiler (2006), The Southern Hemisphere Westerlies in a warming world: Propping open the door to the deep ocean, *J. Clim.*, *19*, 6382–6390.

Sarmiento, J. L., and N. Gruber (2006), *Carbon cycle, in Ocean Biogeochemical Dynamics*, chap. 8, pp. 318–358, Princeton Univ. Press, Princeton, N. J.

Schlitzer, R. (2000), Applying the adjoint method for biogeochemical modeling: Export of particulate organic matter in the World Ocean, in *Inverse Methods in Biogeochemical Cycles*, *Geophys. Monogr. Ser.*, vol. 114, edited by P. Kasibhatla et al., pp. 107–124, AGU, Washington, D. C.

Shackleton, N. (1977), Carbon-13 in uvigerina: Tropical rainforest history and the equatorial Pacific carbonate dissolution cycles, in *The Fate of Fossil Fuel CO_2 in the Ocean*, edited by N. Andersen and A. Malahoff, pp. 401–428, Plenum, New York.

Shulmeister, J., et al. (2004), The Southern Hemisphere westerlies in the Australasian sector over the last glacial cycle: A synthesis, *Quat. Int.*, *118-119*, 23–53.

Siddall, M., T. F. Stocker, G. M. Henderson, F. Joos, M. Frank, N. R. Edwards, S. Ritz, and S. A. Müller (2000), Modelling the relationship between $^{231}Pa/^{230}Th$ distribution in North Atlantic sediment and Atlantic Meridional Overturning Circulation, *Paleoceanography*, *22*, PA2214, doi:10.1029/2006PA001358.

Sigman, D. M., and E. A. Boyle (2000), Glacial/interglacial variations in atmospheric carbon dioxide, *Nature*, *407*, 859–869.

Sigman, D., S. Jaccard, and G. Haug (2004), Polar ocean stratification in a cold climate, *Nature*, *428*, 59–63.

Talley, L. D., J. L. Reid, and P. E. Robbins (2003), Data-based meridional overturning streamfunctions for the global oceans, *J. Clim.*, *16, 3213–3226*.

Thompson, D. W. J., and S. Solomon (2002), Interpretation of recent Southern Ocean climate change, *Science*, *296*, 895–899.

Toggweiler, J. (1999), Variation of atmospheric CO_2 by ventilation of the ocean's deepest water, *Paleoceanography*, *14*, 571–588.

Toggweiler, J. R., and B. Samuels (1995), Effect of Drake Passage in the global thermohaline circulation, *Deep Sea Res., Part I*, *42*, 477–500.

Toggweiler, J. R., A. Gnanadesikan, S. Carson, R. Murnane, and J. L. Sarmiento (1995), Representation of the carbon cycle in box models and GCMs: 1. Solubility pump, *Global Biogeochem. Cycles*, *17*(1), 1026, doi:10.1029/2001GB001401.

Toggweiler, J. R., J. Russell, and S. Carson (2006), Midlatitude westerlies, atmospheric CO_2, and climate change during ice ages, *Paleoceanography*, *21*, PA2005, doi:10.1029/2005PA001154.

Treguer, P., D. M. Nelson, A. J. V. DeMaster, A. Leynart, and B. Queguiner (1995), The silica balance in the world ocean: A reestimate, *Science*, *268*, 375–379.

Volk, T., and M. I. Hoffert (1985), Ocean carbon pumps: Analysis of relative strengths and efficiencies in ocean driven atmospheric pCO_2 changes, in *The Carbon Cycle and Atmospheric* CO_2*: Natural Variations Archean to Present*, *Geophys. Monogr. Ser.*, vol. 32, edited by E. T. Sundquist and W. S. Broecker, pp. 99–110, AGU, Washington, D. C.

Watson, A. J., and A. C. Naveira Garabato (2006), The role of Southern Ocean mixing and upwelling in glacial-interglacial atmospheric CO_2 change, *Tellus, Ser. B*, *58*, 73–87.

Wyrwoll, K.-H., D. Buwen, and P. Valdes (2000), On the position of Southern Hemisphere westerlies at the Last Glacial Maximum: An outline of AGCM simulation results and evaluation of their implications, *Quat. Sci. Rev.*, *19*, 881–898.

F. Joos, P. Parekh, and T. Tschumi, Climate and Environmental Physics, Physics Institute, University of Bern, Sidlerstrasse 5, CH-3012 Bern, Switzerland. (tschumi@climate.unibe.ch)

How important are Southern Hemisphere wind changes for low glacial carbon dioxide? A model study – supplementary material

T. Tschumi, F. Joos and P. Parekh,
Climate and Environmental Physics,
Physics Institute, University of Bern,
Sidlerstrasse 5, CH-3012 Bern,
Switzerland.

Supplementary material for "How important are Southern Hemisphere wind changes for low glacial carbon dioxide? A model study" by T. Tschumi, F. Joos and P. Parekh, *Paleoceanography*, 2008, doi:10.1029/2008PA001592.

1 Parametrization of organic matter, opal and $CaCO_3$ production

In the biogeochemical component of the Bern3D model euphotic zone depth is uniformly set to 75 meters. Biological consumption of phosphate Γ_{new} is limited by temperature, the availability of light (I), phosphate (PO_4) and iron (Fe) and is parametrized following *Doney et al.* [2006]:

$$\Gamma_{new} = \frac{T+2}{T+10} F_I \min\left(F_{PO_4}, F_{Fe}\right) \min\left(PO_4, \frac{Fe}{\mathcal{R}_{Fe:P}}\right) \frac{1}{\tau}, \tag{1}$$

$$F_I = \frac{I}{I+\kappa_I},\ F_{PO_4} = \frac{PO_4}{PO_4+\kappa_{PO_4}},\ F_{Fe} = \frac{Fe}{Fe+\kappa_{Fe}}. \tag{2}$$

T stands for temperature in degrees Celsius, I for insolation, κ_{Fe} and κ_{PO_4} are the half-saturation constants for PO_4-uptake with respect to phosphate and iron respectively. τ represents the biomass turnover timescale set here to 30 days. $\mathcal{R}_{Fe:P}$ is the ratio of Fe- to PO_4-uptake. A fraction $\sigma = \frac{2}{3}$ of biological productivity Γ_{new} enters the DOP-pool, which decays into its mineral constituents with an e-folding lifetime $\tau_{DOP} = 0.5$ yrs (*Yamanaka and Tajika* [1997]). The remaining fraction $\Gamma_{new}(1-\sigma)$ is exported out of the euphotic zone as sinking particulate organic matter (POM) and is instantaneously remineralized in the water column beneath. The downward flux of phosphate $F_{PO_4}(z)$ is scaled according to the empirical power law profile of *Martin et al.* [1987]:

$$F_{PO_4}(z) = \int\limits_{z'=z_{euphotic}}^{0} (1-\sigma)\Gamma_{new}(z')dz' \left(\frac{z}{z_{euphotic}}\right)^{-\alpha} \quad for\ z > z_{euphotic} \tag{3}$$

The remaining POM-flux at the bottom of the ocean is remineralized in the deepest box. Biologically driven fluxes of carbon, alkalinity, oxygen and iron are linked to those of phosphorous using fixed elemental ratios in organic matter ($\mathcal{R}_{C:P}, \mathcal{R}_{Alk:P}, \mathcal{R}_{O_2:P}, \mathcal{R}_{Fe:P}$).

The oceanic iron-cycle is represented in the model following *Parekh et al.* [2007]. Dissolved iron is partitioned into free, Fe', and complexed, FeL, forms assuming that the total organic ligand concentration is uniform and thermodynamic equilibration is rapid. Iron enters the ocean through aoelian deposition and is removed therefrom by scavenging.

Modeled production of $CaCO_3$ and opal shells depends on biological productivity Γ_{new} and on availability of silicic acid. In silicic acid replete conditions, opal production through growth of diatoms Γ_{opal} is favored at the expense of $CaCO_3$ production $\Gamma_{calcite}$. The following formulations adopted from the HAMOCC5 model (*Maier-Reimer et al.* [2005]) are used to represent this competition:

$$\Gamma_{opal} = \min(\Gamma_{new}(1-\sigma)R^D_{Si:P}\frac{Si}{K^D_{Si}+Si}, 0.5Si), \tag{4}$$

$$\Gamma_{calcite} = R^{calc}_{Ca:P}\min(M_{CaCO_3}\Gamma_{new}(1-\sigma), \Gamma_{new}(1-\sigma) - \frac{\Gamma_{opal}}{R^D_{Si:P}}), \tag{5}$$

where Γ_{opal} is in units $\frac{molSi}{m^3s}$ and $\Gamma_{calcite}$ is in $\frac{molC}{m^3s}$. $R^D_{Si:P}$ is the ratio of silicate to phosphorous in diatoms, K^D_{Si} is the half-saturation constant for silicate uptake in diatoms, M_{CaCO_3} is the maximum rain-ratio and $R^{calc}_{Ca:P}$ stands for the calcium to phosphorous ratio in calcifiers.

Observations indicate that half-saturation constants for silica-uptake in diatoms K^D_{Si} vary significantly in the real ocean (*Martin-Jézéquel et al.* [2000], *Sommer* [1986]). Therefore K^D_{Si} is prescribed in the model as a function of the local yearly maximum silicate concentration, Si_{max}, following *Aumont and Bopp* [2006]:

$$K^D_{Si} = K^{min}_{Si} + K^{max}_{Si}\frac{Si^2_{max}}{(K^{D*}_{Si})^2 + Si^2_{max}} \tag{6}$$

Depending on light-, silicate-, phosphorous- and iron-availability, diatoms assimilate variable amounts of silicate to build up their frustules (*Sarthou et al.* [2005]). Thus the ratio of silicate to phosphorous in diatoms $R^D_{Si:P}$ is computed following *Aumont and Bopp* [2006]:

$$R^D_{Si:P} = R^*_{Si:P}\frac{[Si]}{K^D_{Si}+[Si]}(5.4\exp(-4.23min(F_I, F_{PO_4}, F_{Fe})) + 1.13), \tag{7}$$

where the light-, phosphorous- and iron-limitation terms F_I, F_{PO_4} and F_{Fe} are calculated as in equation (1).

Opal and $CaCO_3$ are instantaneously exported from the euphotic zone and redissolved in the water-column beneath the site of production. Downward fluxes are assumed to decrease exponentially with length-scale $l_{opal} = 10$ km for opal and $l_{calcite} = 3.5$ km for $CaCO_3$:

$$F_{opal/calcite}(z) = \int_{z'=z_{euphotic}}^{0} (1-\sigma)\Gamma_{opal/calcite}(z')dz' \exp\left(-\frac{z - z_{euphotic}}{l_{opal/calcite}}\right) for\ z > z_{euphotic} \tag{8}$$

The remaining fluxes of opal and $CaCO_3$ at the ocean bottom are redissolved in the deepest box.

2 Model Representation of Additional Mechanisms

2.1 CO_2 Solubility

To estimate the effect of increased CO_2 solubility we impose a reconstruction of LGM SST and SSS on the carbonate chemistry routine that calculates the speciation of DIC and pCO_2 in the sea surface. Note that the temperature and salinity fields relevant to ocean dynamics are kept unchanged. The fields for glacial SST and SSS are derived through interpolation from the data set provided by *Paul and Schäfer-Neth* [2003] which is a merge of CLIMAP and GLAMAP data with modeling results.

2.2 Sea Ice Cover

In glacial times, increased sea ice cover around Antarctica might have decreased outgassing of CO_2 in the Southern Ocean. Using a box model, *Stephens and Keeling* [2000] have demonstrated a substantial lowering of atmospheric CO_2 resulting from reduced air-sea gas exchange in the Antarctic region. However, *Archer et al.* [2003] showed that in contrast to box models, such an effect cannot be found in GCMs. In this study we examine the mechanism by reducing gas exchange in the domain around Antarctica where sea ice was present at the Last Glacial Maximum (LGM). Based on the data set provided by *Paul and Schäfer-Neth* [2003] a monthly map of fractional sea ice cover was obtained through area-weighted interpolation onto the coarse Bern3D model grid. Fractional sea ice cover was then used to linearly scale down gas transfer velocities according to:

$$k_w^{ice} = (1 - f_{ice}) k_w^{open}, \tag{9}$$

where k_w^{open} denotes the gas transfer velocity for an open ocean surface and f_{ice} is the fractional sea ice cover. Circulation and biological uptake were held unaffected by the addition of sea ice.

2.3 $CaCO_3$ Compensation

The mechanism of $CaCO_3$ compensation calls for a deep ocean drop in CO_3^{2-} due to an addition of excess remineralized CO_2 from the upper ocean (*Marchitto et al.* [2004]). The resulting decline in the saturation of deep waters with respect to $CaCO_3$ initiates the dissolution of seafloor $CaCO_3$ sediments. This process adds alkalinity and DIC to the seawater in a 2:1 ratio and thus shifts the speciation of DIC away from dissolved CO_2. When this signal propagates to the ocean surface, pCO_2 is reduced, causing a further uptake of atmospheric CO_2.

$CaCO_3$ compensation acts as homeostat for the deep ocean carbonate concentration. We simulate the effect of this process by restoring CO_3^{2-} at the sea floor deeper than 2000 meters towards CO_3^{2-*}, the carbonate concentrations diagnosed in the initial state:

$$J^{sed}_{CO_3^{2-}}(i,j,k_{i,j}) = \begin{cases} \frac{1}{\tau_{rest}}(CO_3^{2-*}(i,j,k_{i,j}) - CO_3^{2-}(i,j,k_{i,j})), \\ \text{if depth}(k_{i,j}) \ > \ 2000\text{m}, \\ \\ 0, \ \text{otherwise.} \end{cases} \tag{10}$$

$$SMS^{sed}_{DIC}(i,j,k_{i,j}) = J^{sed}_{CO_3^{2-}}(i,j,k_{i,j}) \tag{11}$$

$$SMS^{sed}_{ALK}(i,j,k_{i,j}) = 2J^{sed}_{CO_3^{2-}}(i,j,k_{i,j}) \tag{12}$$

SMS_{DIC}^{sed} and SMS_{ALK}^{sed} are the source-minus-sink terms for DIC and alkalinity that result from sediment dissolution or accumulation. The restoring timescale τ_{rest} is set to 10 years as we are not interested in the transient response, but want to bring the model into the new equilibrium as quickly as possible. The latitudinal and meridional indices of the model grid are denoted by i and j, while $k_{i,j}$ represents the depth-index of the deepest ocean grid cell above the sea floor.

2.4 Terrestrial Carbon Release

Terrestrial carbon release (*Crowley* [1995], *Bird et al.* [1994], *Shackleton* [1977]) is simulated by injecting 500 GtC into the atmosphere. This is done by instantaneously increasing atmospheric CO_2 by 236 ppm.

References

Archer, D. E., P. A. Martin, J. Milovich, V. Brovkin, G.-K. Plattner, and C. Ashendel (2003), Model sensitivity in the effect of Antarctic sea ice and stratification on atmospheric pCO_2, *Paleo.*, *18*, PA1012, doi:doi:10.1029/2002PA000760.

Aumont, O., and L. Bopp (2006), Globalizing results from ocean in situ iron fertilization studies, *Global Biogeochem. Cycles*, *20*, GB2017, doi:10.1029/2005GB002591.

Bird, M. I., J. Lloyd, and G. D. Farquhar (1994), Terrestrial carbon storage at the lgm, *Nature*, *371*, 566.

Crowley, T. (1995), Ice age terrestrial carbon changes revisited, *Global Biogeochem. Cycles*, *9*(3), 377389.

Doney, S. C., K. Lindsay, I. Fung, and J. John (2006), Natural variability in a stable 1000 year global coupled climate-carbon cycle simulation, *J. Climate*, *19*, 3033–3054.

Maier-Reimer, E., I. Kriest, J. Segschneider, and P. Wetzel (2005), The HAMburg Ocean Carbon Cycle model HAMOCC5.1 - technical description release 1.1, *Tech. rep.*, Max Planck Institue for Meteorology.

Marchitto, T. M., J. Lynch-Stieglitz, and S. R. Hemming (2004), Deep Pacific $CaCO_3$ compensation and glacial-interglacial atmospheric CO_2, *Earth and Planetary Science Letters*, *231*, 317–336.

Martin, J., G. Knauer, D. Karl, and W. Broenkow (1987), VERTEX: Carbon cycling in the northeast Pacific, *Deep Sea-Res.*, *34*, 267–285.

Martin-Jézéquel, V., M. Hildebrand, and M. Brezinski (2000), Silicon metabolism in diatoms: Implications for growth, *Journal of Phycology*, *36*, 1–20.

Parekh, P., F. Joos, and S. A. Müller (2007), The role of aeolian iron flux in controlling carbon dioxide fluctuations during Antarctic warm events, *Paleo.*, submitted.

Paul, A., and C. Schäfer-Neth (2003), Modeling the water masses of the Atlantic Ocean at the Last Glacial Maximum, *Paleo.*, *18*, PA1058, doi:doi:10.1029/2002PA000783.

Sarthou, G., K. Timmermans, S. Blain, and P. Treguer (2005), Growth physiology and fate of diatoms in the ocean: a review., *J. of Sea Research*, *53*, 25–42.

Shackleton, N. (1977), Carbon-13 in uvigerina: Tropical rainforest history and the equatorial Pacific carbonate dissolution cycles, in *The Fate of Fossil Fuel CO_2 in the Ocean*, edited by N. Andersen and A. Malahoff, pp. 401–428, Plenum, New York.

Sommer, U. (1986), Nitrate and silicate competition among antarctic phytoplankton, *Mar. Biol.*, *91*, 345–351.

Stephens, B., and R. Keeling (2000), The influence of Antarctic sea ice on glacial-interglacial CO_2 variations, *Nature*, *404*, 171–174.

Yamanaka, Y., and E. Tajika (1997), Role of dissolved organic matter in the marine biogeochemical cycles: Studies using an ocean biogeochemical general circulation-model, *Global Biogeochem. Cycles*, *4*, 599–612.